Michigan State University

National Superconducting Cyclotron Laboratory

IMPACT PARAMETER SELECTED EXCITED STATE POPULATIONS FOR $^{36}Ar + ^{197}Au$ REACTIONS AT E/A = 35 MeV

F. ZHU, W.G. LYNCH, D.R. BOWMAN, R.T. deSOUZA,
C.K. GELBKE, Y.D. KIM, L. PHAIR, M.B. TSANG,
C. WILLIAMS, and H.M.XU

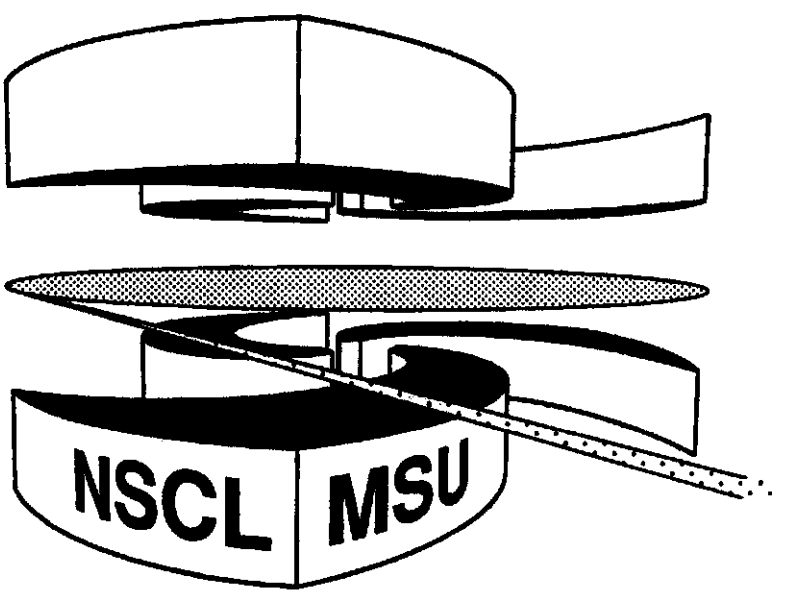

MSUCL-985

MAY 1995

Impact Parameter Selected Excited State Populations for ^{36}Ar + ^{197}Au Reactions at E/A = 35 MeV

F. Zhu", W.G. Lynch, D.R. Bowman*, R.T. de Souza[c], C.K. Gelbke, Y.D. Kim[d], L.Phair[e], M.B.Tsang, C.Williams, and H.M.Xu[f]

National Superconducting Cyclotron Laboratory and Department of Physics
Michigan State University
East Lansing, Michigan 48824

Abstract

Impact parameter selected excited state populations were measured for ^{36}Ar + ^{197}Au reactions at E/A=35 MeV in order to better understand population inversions observed in a previous measurement of ^{14}N + Ag reactions at E/A=35 MeV. The present impact parameter selected measurements revealed such population inversions to be most prominent in low multiplicity peripheral reactions. The excited state population for central collisions approach statistical model predictions for T $\approx$ 4 MeV.

PACS numbers: 25.70.Mn, 25.70.Gh

I. Introduction

In energetic nucleus-nucleus collisions, very hot and dilute nuclear systems can be created which decay on time scales commensurate with nuclear relaxation times [1-5]. These transient excitations offer singular opportunities for determining the statistical properties of hot nuclei [2, 3] and hot nuclear matter [4-8].

In this paper, we are concerned with questions concerning the validity of the approximation of local thermal equilibrium for preequilibrium production mechanisms and with the internal excitation of fragments produced therein. If local thermal equilibrium is achieved in one of these transient excitations, the corresponding emission temperature can be obtained from measurements of the population of excited states [1, 5, 9]. While cross calibrations of this technique have been performed via measurements of the excited states of fragments emitted from equilibrated heavy residues [9-14], the major utility of this technique lies in its ability to provide information about the internal excitation of fragments produced via preequilibrium process for which alternative measures of the internal excitation do not exist. Such processes are known to play a major role in the multifragment disintegration of highly excited systems produced in central collisions between heavy nuclei [4-8]; there, questions concerning the degree of thermalization have a significant impact upon efforts to extract information about phase transitions in low density nuclear matter [3,4]. Systematic studies of emission temperatures for preequilibrium processes indicate a gradual increase in the emission temperature from $T_{em} \approx 3$ MeV to $T_{em} \approx 6$ MeV with incident energy over the energy range of $E/A = 20 - 200$ MeV [1,5,15-24]. A recent test of this local thermal equilibrium assumption for the $^{14}N + {}^{nat}Ag$ reaction at E/A = 35 MeV, however, revealed non-statistical excited state populations of emitted intermediate mass fragments(IMF's : Z = 3-20), including inversions of the populations for specific excited states of ^{10}B fragments

[22, 23]. Since this latter measurement was performed without impact parameter selection, there are some questions whether these observations are related to the dominance of large impact parameter collisions by non-equilibrium transport phenomena [25, 26, 27, 28]. To explore this issue further, we measured ^{10}B and other IMF particle unbound excited state populations for the ^{36}Ar + ^{197}Au reaction at E/A = 35 MeV, in conjunction with a charged particle multiplicity filter. Some aspects of this work were published earlier [24].

This particular ^{36}Ar +^{197} Au system has been extensively investigated with a low-threshold 4π charged particle detector array covering the angular range of $16^o \leq \Theta_{Lab} \leq 160^o$ [29]. In peripheral collisions, fragment emission is a fairly unlikely process; the average IMF multiplicity increases from $< N_{IMF} > \lesssim 0.1$ for $N_C = 2$ to $< N_{IMF} > \approx 1.2$ for $N_C \geq 15$ [29]. The elemental distributions observed for various cuts on charged-particle multiplicity exhibit a nearly exponential falloff as a function of the fragment charge [29] which can easily be reproduced by statistical calculations [30, 31, 32, 33]. The inclusive element distributions are rather similar to those observed in central collisions, and the exponential falloff is only slightly steeper for fragments produced in peripheral collisions [29]. At forward angles the energy spectra of fragments produced in peripheral collisions exhibit a high-energy shoulder which are reminiscent of damped collisions or emission from a projectile-like source [29]. This shoulder was not observed in energy spectra gated on central collisions, for which the spectra exhibit nearly exponential slopes [29].

Analysis of energy spectra for fragments permitted estimates of the contributions from preequilibrium and equilibrium emission mechanisms. At forward angles, the fragment yields predominantly originate from preequilibrium emission mechanisms even to rather low emission energies [29]. Average emission time scales of $\tau = 100 - 200$fm/c were extracted from inclusive mixed fragment correlation functions constructed for fragments emitted at angles

$16^o \leq \Theta_{Lab} \leq 31^o$ [29]. Only modest dependencies were observed for various cuts on charged particle or IMF multiplicity [29]. For the most peripheral collisions with $N_C \leq 7$ even shorter time scales were observed that are inconsistent with fragment emission from an equilibrated projectile-like residue [29]. In this reaction, one observes short breakup time scales at the same time one observes fragment charge distributions that are consistent with a phase space dominated statistical process.

In this paper we test in detail whether the fragment production mechanisms for this $^{36}Ar + ^{197}Au$ reaction at E/A=35 are consistent with the concept of local thermal equilibrium. The experimental details are given in section II. Information about the impact parameter selection is discussed in section III and impact parameter selected single particle data are presented in section IV. Excited state populations and the emission temperatures are presented in section V. Sequential decay calculations are performed in section VI and the calculated temperatures are compared with data in section VII. Previous results on ^{10}B excited states measurement [24] will be explored in greater detail. Summary and conclusions are given in section VIII.

II. Experimental Details

In the experiment, a 1.0 mg/cm^2 thick ^{197}Au target was bombarded with a 1260 MeV ^{36}Ar beam produced by the K500 cyclotron of the National Superconducting Cyclotron Laboratory at Michigan State University. A high resolution hodoscope was used to measure the excited state populations for ^{10}B and other particle unstable intermediate mass fragments [34]. The MSU Miniball 4π array was used as an impact parameter filter [29, 35]. The high resolution hodoscope consisted of 13 closely-packed $\Delta E - E$ telescopes, centered at $\Theta_{lab} = 39^o$. Nine telescopes, each having a solid angle of 3.6 msr, consisted of a 150 μm surface-barrier silicon ΔE-detector, a 5mm lithium-drifted silicon E-detector (Si(Li)) and a

400 μm silicon-surface barrier veto detector. Each 5 mm Si(Li) detector was fabricated with a total dead layer less than 15 μm. The dynamic range of these telescopes was optimized to isotopically resolve particles with Z$\leq$4. The remaining four telescopes, each having a solid angle of 5.6 msr, consisted of 75 μm and 100 μm thick surface-barrier silicon ΔE-detectors and a 5 mm lithium-drifted Si(Li) E-detector. Here, the dynamic range was optimized to isotopically resolve particles with Z$\geq$2. The position information for each individual telescope was obtained with two single-wire proportional gas-counters, placed at the front of the telescope, each providing one coordinate of the x-y read out. A position resolution better than 0.3mm FWHM was achieved for alpha particles from a point ^{244}Cm source placed at the target position. Energy calibrations were performed by extrapolating pulses from a ^{241}Am alpha source using a precision pulser system. Gain shifts of the electronics during the experiment were monitored by pulsers applied to the test inputs of the preamplifiers.

The MSU 4π Miniball array was used in the experiment to provide an impact parameter filter. Rings 2-11 of the array [35] were used. These rings, when complete, have 176 detectors and cover an angular range of 16^0 - 160^0 in the laboratory with the solid angle coverage of 85% of 4π. In order to fit the hodoscope into the Miniball array, 27 out of the 176 phoswich detectors in rings 2-11 of the original array were removed to allow the insertion of the hodoscope. The remaining Miniball array covered a solid angle corresponding to 77% of 4π.

Each phoswich detector of the 4π Miniball array consisted of a 40 μm thin fast plastic scintillator foil and a 2 cm CsI crystal and provided charged particle detection and particle identification with a low energy threshold. Particle identification was achieved by integrating the photomultiplier signal over several distinct timing gates. In this experiment, slow moving heavy particles which stopped in the fast plastic scintillator were not analyzed. The threshold for particle detection and identification in the Miniball was about $E/A \approx$ 2, 3, 4 MeV for

Z = 3, 10, and 18 fragments. Further details about the Miniball 4π array are given in refs. [29, 35].

III. Impact parameter selection

For ^{36}Ar + ^{197}Au collisions at E/A = 35 MeV, an impact parameter filter has been constructed using the total charged particle multiplicity detected in the original 176 detector Miniball which covered a solid angle corresponding to 85% of 4π [29]. Such impact parameter filters can provide a moderately accurate impact parameter selection for small impact parameters with large associated charged particle multiplicities but suffer some loss of sensitivity for peripheral collisions at large impact parameters where the charged particle multiplicity may be small or vanishing. The top panel of Figure 1 was taken from ref. [29] and shows the detected total charged particle multiplicity distribution for that experiment. A monotonic relationship has been assumed between the multiplicity and the impact parameter in order to assign the impact parameter using the measured total charged particle multiplicity. This can be easily expressed as an integral relationship,

$$(b/b_{max})^2 = \int_{N_c}^{\infty} [dP(N_c')/dN_c'] \cdot dN_c', \tag{1}$$

where b_{max} corresponds to the maximum impact parameter for particles detected in the Miniball ($N_c \geq 1$). $dP(N_c)/dN_c$ is the normalized probability distribution for the charged particle multiplicity N_c shown in the top of Figure 1. It is normalized such that $\int_1^{\infty}[dP(N_c)/dN_c] \cdot dN_c = 1$. The bottom panel of Figure 1 shows the relationship between the total charged particle multiplicity and the impact parameter obtained from Equation 1. Further details can be found in ref. [29].

It is useful to construct an impact parameter filter for the Miniball-Hodoscope coincidence experiment which is equivalent to the impact parameter filter shown in Figure 1. To

complicate this connection, however, the trigger conditions of the two experiments are different. The multiplicity distribution in Figure 1 was obtained with a trigger which requires one or more charged particles in the original Miniball, while the Miniball-Hodoscope coincidence experiment used a subset of Miniball, and also required at least one more particle in the Hodoscope as well.

Nevertheless, it is straightforward to cross calibrate the multiplicity filters of the two experiments, using data taken from the Miniball stand-alone experiment with the original array [29]. In this exercise, it is important to select events from the Miniball stand-alone experiment which are equivalent to those measured in the Miniball-Hodoscope coincidence experiment. Several steps were taken to make this correspondence.

1. For this analysis of the Miniball stand-alone experiment, we removed those detectors which were removed in the Miniball-Hodoscope coincidence experiment.

2. Some of these detectors (thereafter termed " pseudo-hodoscope detectors ") which were at the appropriate angles were chosen to mimic the hodoscope telescopes.

3. We require the detection of at least one particle in these pseudo-hodoscope telescopes.

4. The resulting associated multiplicity N_A in the Miniball could then be plotted as a function of the total charged particle multiplicity in the total array N_c to obtain the correspondence between the two quantities. In this way one could calibrate the impact parameter filter based upon the associated charged particle multiplicity detected in the smaller Miniball array.

In Figure 2, we show the correlation between the mean total charged particle multiplicity $< N_c >$ and associated multiplicity N_A for events in which a ^{10}B nucleus is detected

in the pseudo-hodoscope detectors. On the right hand side, we show the impact parameter assignment deduced from the relationship between N_c and b/b_{max} in Figure 1.

Figure 3 illustrates the influence of detecting a ^{10}B nucleus in the hodoscope upon the charged particle multiplicity distribution and on the impact parameter. The solid squares indicate the probability of observing a charged particle multiplicity N_A in the Miniball in coincidence with the detection of a ^{10}B nucleus in the hodoscope. The dashed line indicates the corresponding inclusive multiplicity distribution obtained from the data of ref. [29], arbitrarily normalized, which was obtained with that part of Miniball which was used as an impact parameter filter, but without the additional requirement of the detection of a ^{10}B nucleus in the hodoscope. In the case of events triggered with a ^{10}B nucleus, the probability of having very high multiplicity events is reduced, possibly reflecting the fact that ^{10}B takes away energy, leaving less excitation energy for particle emission. This interpretation is supported by the associated multiplicity distribution corresponding to the detection of one proton in the hodoscope, shown by the open circles. In this case, the protons carry away less energy and have an associated multiplicity distribution which deviates less from the inclusive multiplicity distribution (dashed line). For both events gated on protons and ^{10}B's, the detection of one charged particle in the Hodoscope suppresses peripheral reactions greatly. This suppression is stronger for the ^{10}B trigger than for the proton trigger, consistent with previous observations [29]. The solid circles in Figure 3 show the corresponding multiplicity distribution for correlated ^{6}Li and α particles detected in the hodoscope. Both the ^{10}B (solid squares) and $\alpha - ^{6}Li$ (solid circles) trigger conditions appear to corresponding to equivalent impact parameters.

The impact parameter selection gates, indicated by the dashed-dotted lines, were used later on to distinguish **peripheral** ($N_A \leq 5$) and **central** collisions ($N_A \geq 10$) collisions.

Also shown at the top of the figure is the impact parameter scale which was obtained from Figure 2 using Equation 1.

IV. Impact parameter selected single particle cross section

As an example, Figure 4 shows the energy spectra for ^{10}B nuclei detected at 45^0 in the high resolution hodoscope, for low multiplicity (solid points) and high multiplicity (solid squares) events in the Miniball. Similar spectra are shown in Figure 5 for helium, lithium and beryllium isotopes for peripheral (left panel) and central (right panel) reactions. The energy spectra for peripheral collisions extend to higher energies than the energy spectra for central collisions. This suggests a greater degree of thermalization for central collisions.

In order to get a reasonable parameterization for the cross section for later calculations of the detection efficiency, the energy spectra were fitted with non-relativistic Maxwell distributions, assuming three moving sources of the form,

$$\frac{d^2\sigma}{d\Omega dE} = \sum_{i=1}^{3} N_i \sqrt{E - V_c} e^{-E_{si}/T_i}, \tag{2}$$

with $E_{si} = E - V_c + E_i - 2\sqrt{E_i(E - V_C)}\cos\theta$. Here V_c is a Coulomb barrier parameter, T_i is the temperature parameter for the emitting source, $E_i = \frac{1}{2}mv_i^2$, where m is the mass of the detected particle, v_i is the velocity of the source in the laboratory frame and θ is the angle of the emitted particle in the laboratory frame. The solid lines in Figure 4 and Figure 5 depict three source fits. The fitting parameters are listed in Table 1. It is important to note that, due to the limited angular coverage range of the data in Figure 4 and Figure 5, the moving source parameters in Table 1 are not reliable for extrapolation to scattering angles which lie outside the angular range covered by the Hodoscope. These parameters are only useful as input to the efficiency calculations to extract the population probabilities in section VI.

V. Temperature measurements of excited nuclear systems

The population of excited states of fragments are extracted as follows [17]. Suppose a fragment A in an excited state with excitation energy E* decays to two daughter nuclei b and c,

$$A^* \rightarrow b + c. \tag{3}$$

This decay can be observed by measuring fragments b and c in coincidence. From the energies and angles of particle b and c in the laboratory frame, the excitation energy E* of the parent nucleus in its rest frame can be deduced and from many events, a decay spectrum can be constructed. The experimentally measured decay spectrum $Y_{exp}(E^*_{mea})$ consists of two parts,

$$Y_{exp}(E^*_{mea}) = Y_c(E^*_{mea}) + Y_b(E^*_{mea}). \tag{4}$$

Here, $Y_c(E^*_{mea})$ is the decay spectrum for the correlated decay products from the particle unstable parent fragment A, and $Y_b(E^*_{mea})$ is the background from pairs of particles which do not originate from parent fragment A. While the detailed calculation of the background yields from first principles requires an extremely detailed knowledge of final state interactions, analysis shows that Y_b can be accurately parameterized by, [34]

$$Y_b(E) = C_{12}(1 - exp^{-(E-E_b)/\Delta})Y_1 \cdot Y_2 \cdot \Theta(E - E_b). \tag{5}$$

Here, E_b is the threshold for the decay $A^* \rightarrow b + c$ and Δ is the width of the suppression of the background correlation function due to Coulomb final state interactions. Y_1 and Y_2 are the single particle yields of particle b and c, respectively. C_{12} is a normalization constant.

The correlated decay spectrum $Y_c(E^*_{mea})$ of the particle unstable nucleus A* can be written as

$$Y_c(E^*_{mea}) = \int dE^* \epsilon(E^*, E^*_{mea}) \left| \frac{dn(E^*)}{dE^*} \right|_c . \tag{6}$$

Here, E^* is the true excitation energy of nucleus A^*, $dn(E^*)/dE^*$ is the decay spectrum in the rest frame of nucleus A^*, E^*_{mea} is the measured excitation energy and $\epsilon(E^*, E^*_{mea})$ is the efficiency function of the device. The efficiency function $\epsilon(E^*, E^*_{mea})$ was calculated by taking into account the geometry of the hodoscope, the detector energy resolution, the position resolution, the beam spot on target and the constraints on the energy range of particles detected in the hodoscope. The decay of the parent nuclei was assumed to be isotropic in its rest frame. The energy spectrum and angular distribution of the particle unstable parent fragments were assumed to be the same as experimentally measured stable fragments shown in Figure 4 and Figure 5. Therefore, the moving source fitting parameters from Table 1 were used as input to the efficiency function calculations. Further details of efficiency function calculations can be found in ref. [34]. Figure 6 shows the efficiency function calculation for detecting particle unstable ^{10}B nuclei for the ^{36}Ar + ^{197}Au reaction at E/A=35 MeV. The top panel shows the efficiency of the hodoscope and the bottom panel shows the excitation energy resolution (RMS) of the hodoscope as the functions of the relative energy between the α and ^{6}Li particles.

If we assume a thermal population for the excited states of particle unstable fragments and if each state is described by a R-matrix parameterization, the decay yield into a specific channel c in the rest frame of the particle unstable nucleus can be given, [23]

$$\begin{aligned}\left|\frac{dn(E^*)}{dE^*}\right|_c &= \sum_\lambda \frac{dn_\lambda(E^*)}{dE^*} \cdot \frac{\Gamma_{\lambda c}}{\Gamma_\lambda} \\ &= \sum_\lambda N_\lambda \cdot e^{-E^*/T} \cdot \frac{2J_\lambda + 1}{\pi} \cdot \frac{\Gamma_\lambda/2}{(E_\lambda + \Delta_\lambda - E^*)^2 + \Gamma_\lambda^2/4} \\ &\quad \times \left[1 - \frac{d\Delta_\lambda}{dE^*} + \frac{E_\lambda + \Delta_\lambda - E^*}{\Gamma_\lambda} \cdot \frac{d\Gamma_\lambda}{dE^*}\right] \cdot \frac{\Gamma_{\lambda c}}{\Gamma_\lambda}. \end{aligned} \quad (7)$$

Here, J_λ, E_λ, Γ_λ, Δ_λ, and $\Gamma_{\lambda c}/\Gamma_\lambda$ are the spin, energy, total width, energy shift and branching

ratio for the decay of resonance λ into channel c at excitation energy E*. $dn_\lambda(E^*)/dE^*$ is the excitation energy spectrum for level λ and N_λ is a constant that is determined by fitting the excitation energy spectrum and which should be independent of λ for a system in local thermal equilibrium.

For narrow levels, Γ_λ and Δ_λ can be treated as energy independent, and the R-matrix decay spectra can be further simplified to the Breit-Wigner formula,

$$\left|\frac{dn_\lambda(E^*)}{dE^*}\right|_c = \sum_\lambda N_\lambda \cdot e^{-E^*/T} \cdot \frac{2J_\lambda + 1}{\pi} \cdot \frac{\Gamma_\lambda/2}{(E_{res,\lambda} - E^*)^2 + \Gamma_\lambda^2/4} \cdot \frac{\Gamma_{\lambda c}}{\Gamma_\lambda}, \tag{8}$$

with $E_{res,\lambda} = E_\lambda + \Delta_\lambda$. For more complicated cases involving two overlapping states with the same spin and parity, a modified R-matrix formula can be obtained [23].

The excitation energy spectrum, after folding with the efficiency function using equation 6, provides a theoretical expression for the coincidence yields. Combining this with the background parameterization of equation 5, the experimentally measured decay spectrum can be fitted to obtain the population probability n_λ for each level. Assuming that each m sub-state of level λ is populated equally, the population probability for each m sub-state of level λ is obtained by integrating the excitation energy spectrum for level λ over excitation energy [23],

$$n_\lambda = \frac{1}{2J_\lambda + 1} \int dE^* \frac{dn_{\lambda,tot}(E^*)}{dE^*}. \tag{9}$$

For most of the excited states considered, the excited states are sufficiently narrow that the Boltzmann factor, $e^{-E^*/T}$, varies little over the resonance and can be approximated at the resonance energy $e^{-E_{res,\lambda}/T}$, and taken out of the integral. The population probability then becomes,

$$n_\lambda = N_\lambda e^{-E_{res,\lambda}/T}. \tag{10}$$

In this case, the Breit-Wigner formula for a group of levels can be written as,

$$\left|\frac{dn(E^*)}{dE^*}\right|_c = \sum_\lambda n_\lambda \frac{2J_\lambda + 1}{\pi} \cdot \frac{\Gamma_\lambda/2}{(E_{res,\lambda} - E^*)^2 + \Gamma_\lambda^2/4} \cdot \frac{\Gamma_{\lambda c}}{\Gamma_\lambda}. \quad (11)$$

Decay of ^{10}B excited states with impact parameter filter

Light nuclei typically have only a few excited states which may be used to extract temperature from population probabilities of excited states. Testing the internal consistency of such a temperature extraction, however, requires the exploration of many excited states to see if they are consistent with a common temperature. For such purposes, we examined ^{10}B nuclei for which many excited states of known spins and parities can be measured [22]. We examined five excited states which decay by the $^{10}B \rightarrow {}^{6}Li + \alpha$ and $^{10}B \rightarrow {}^{9}Be + p$ channels. Previous inclusive measurements of ^{10}B excited states have revealed non-statistical population inversions [22]. By allowing an impact parameter selection, we examined whether these non-statistical population inversions are coming from peripheral collisions [24].

The yields of particle unstable states in ^{10}B nuclei are shown as a function of excitation energy for the $^{10}B \rightarrow {}^{6}Li + \alpha$ and $^{10}B \rightarrow {}^{9}Be + p$ decay channels in the upper and lower halves of Figure 7, respectively. Spectra obtained for peripheral and central collisions are shown in the left and right sides of the figure, respectively. The separation energy E_b for each decay channel and the locations and spins of the relevant particle unstable excited states of ^{10}B nuclei are indicated in the left hand panels of the figure.

The decay spectra for the $^{10}B \rightarrow {}^{6}Li + \alpha$ channel are shown in the upper panels. We analyzed four peaks corresponding to groups of states centered at about $E^* = 4.8$, 5.15, 6.0 and 6.6 MeV. Spectroscopic information about the states located in these groups are given in Table 2. Two excited states of ^{10}B at $E^* = 8.889$ MeV and $E^* = 8.895$ MeV, which decay

to the 3.563 MeV excited state of ^{6}Li by α emission [23], were included in the fitting of the spectrum, but had statistically insignificant yields and were not analyzed further.

The decay spectra for the $^{10}B \rightarrow {}^9Be + p$ decay channel are shown in the lower panels. Here, we extracted the yield from the group of four states at about 7.5 MeV. Other groups of states located at about 6.9, 7.8 and 8.9 MeV were included in the fit, but were not analyzed further because the statistics were insignificant to draw any conclusions. Spectroscopic information about the states located in these groups are also included in Table 2.

The population probabilities, n_λ, were extracted by fitting the coincidence yield, for different assumptions about the background. Reasonable fits were obtained for backgrounds lying within the values bounded by the dashed lines in Figure 7. The normalization parameters C_{12} in Eq. 5 for the backgrounds shown in Figure 7 (and Figures 8-12) are extremely well constrained by the yields at larger relative energies where coincidence yields are completely dominated by the background. The differences between the two background curves in Figure 7 (and Figures 8-12) represent different assumptions about the correction for Coulomb final state interactions approximated here by the parameter Δ. Larger values of Δ than the one used for the lower curve result in a gross underprediction of the yields between peaks corresponding to the groups of excited states at low relative energies wherein the calculated yields lie well outside the error bars of the experimental yields. Smaller values of Δ than the one used for the upper curve result in a gross overprediction of the yields between peaks corresponding to the groups of excited states at low relative energies wherein the calculated yields lie well outside the error bars of the experimental yields. The population probabilities, n_λ, were assumed to be the same within those groups of states in Figure 7, which were not resolved experimentally. The best fits to the coincidence yields, are shown by the solid curves

in Figure 7 and the extracted values for n_λ are given in Table 2.

Excited state populations for ^{5}Li, ^{6}Li, and ^{7}Be fragments.

In addition to ^{10}B fragments, we analyzed several excited states of ^{5}Li, ^{6}Li, and ^{7}Be nuclei to test whether their population probabilities are consistent with local thermal equilibrium. Although each of these nuclei has only one or two excited states which can be analyzed, the overall trends were examined for a global comparison.

The ground state of ^{5}Li is not particle stable; it decays to a proton and an alpha particle, $^5Li \rightarrow p + \alpha$. For such light nuclei system, one can better distinguish the combinatorial background from the resonance peaks by constructing a correlation function,

$$1 + R(E_{rel}) = C_{12}\frac{\sum Y_{12}(\mathbf{p_1}, \mathbf{p_2})}{\sum Y_1(\mathbf{p_1}) \cdot Y_2(\mathbf{p_2})}. \tag{12}$$

Here, $Y_{12}(\mathbf{p_1}, \mathbf{p_2})$ is the coincidence yield of particles 1 and 2 at momenta $\mathbf{p_1}$ and $\mathbf{p_2}$, respectively; $Y_i(\mathbf{p_i})$ is the single particle yield for the ith particle of momenta $\mathbf{p_i}$. E_{rel} is the relative energy between the two particles. The summations in Equation 12 are performed over all momenta consistent with a fixed relative energy E_{rel} and subject to a common multiplicity selection. The constant C_{12} is determined such that $R(E_{rel})$ vanishes at large values of E_{rel} where resonances are not observed.

The $p - \alpha$ correlation function is shown in Figure 8. The left panel shows the results for peripheral collisions and the right panel shows the results for central collisions. The broad peak at $E_{rel} \approx 2$ MeV is from the decay of the ^5Li ground state with spectroscopic parameters $J^\pi = \frac{3}{2}^-, \Gamma = 1.5$ MeV, $\Gamma_c/\Gamma = 1.0$. At low relative energies, there is a narrow peak at $E_{rel} \approx 0.19$ MeV, which is attributed to the decay of ground state of ^9B, $^9B_{g.s} \rightarrow p + {}^8Be_{g.s} \rightarrow$ p + $\alpha + \alpha$ [17, 23]. When we fit the data using the Breit-Wigner formula, a second resonance is included at $E_{rel} = 0.19$ MeV with a decay width of $\Gamma = 0.055$ MeV

to accommodate this process. Because the state at $E_{rel} \approx 2$ MeV is very broad, we include the line shape distortions caused by the Boltzmann factor $exp(-E/T)$, with $T = 4$ MeV, in the fit. The best fit is shown as the solid line in the figure. The two dashed lines shows the upper and lower extremes of the estimated background, which were used to estimate the systematic uncertainty in the background subtraction. Since there is no stable ^5Li ground state, the energy spectra for stable ^6Li were used as input to the efficiency function calculation. Therefore, the extracted population probability in Table 2 is relative to the ^6Li stable yield and has no meaning by itself. It is meaningful only when it is compared to the population probability for the ^5Li excited state at $E^* = 16.66$ MeV. By constructing the ratio of ground and excited state population probabilities, the uncertainty of the efficiency calculation due to lack of stable ^5Li energy spectra largely cancels out.

The excited state of ^{5}Li nuclei at 16.66 MeV decays to a deuteron and a ^3He nucleus. The impact parameter selected $d-\ ^3He$ correlation functions are shown in Figure 9. The left panel shows the spectrum for peripheral collisions and the right panel shows the spectrum for central collisions. The peak near the threshold is from the decay of the 16.66 MeV excited state with spectroscopic parameters $J^\pi = \frac{3}{2}^+, \Gamma = 0.20$ MeV, $\Gamma_c/\Gamma = 0.86$. The R-matrix formalism is used to fit the excited state yield and extract the population probability. The related R-matrix parameters were taken from refs. [23, 36]. In order to fit the excitation energy spectrum, it is necessary to shift the peak 150 KeV higher in excitation energy. This shift may reflect 3-body distortions of the line shape due to Coulomb final state interaction with the target residue [37]. Another wide excited state at $E^* = 20$ MeV was also included in the fit, but was not analyzed further. The extracted population probability in Table 2 for the 16.66 MeV excited state can then be compared to the population probability for the ground state of ^{5}Li to extract an *apparent* temperature. This procedure is discussed later in this paper.

The impact parameter selected correlation functions for the decay of $^6Li \rightarrow d + \alpha$ is shown in Figure 10. The left panel is the data gated on peripheral collisions and the right panel is the data gated on the central collisions. The peak at $E_{rel} \approx 0.71$ MeV is from the decay of the ^6Li excited state at $E^* = 2.186$ MeV with spectroscopic parameters $J^\pi = 3^+, \Gamma = 0.024$ MeV, $\Gamma_c/\Gamma = 1.0$. Also included in the fit is the broad peak at $E_{rel} \approx 3$ MeV, which is from the overlap of two resonances at 4.31 MeV ($\Gamma = 1.7$ MeV, $J^\pi = 2^+$, $\Gamma_c/\Gamma = 0.97$), and 5.65 MeV ($\Gamma = 1.5$ MeV, $J^\pi = 1^+$, $\Gamma_c/\Gamma = 0.74$). We include the line shape distortions caused by the Boltzmann factor $exp(-E/T)$, with $T = 4$ MeV, in the fitting procedure to fit the broad peak better. The solid line depicts the best fit to the data using the Breit-Wigner formalism. The two dashed lines indicate two extreme assumptions for the background which are used to estimate the systematic uncertainty in the fit. The energy spectra for stable ^6Li fragments are used for the efficiency calculation. The population probability in Table 2 is defined relative to the yield of stable ^6Li nuclei. The population probabilities for the pair of states at $E_{rel} \approx 3$ MeV were statistically insignificant compared to the combinatorial background and were not analyzed further.

The impact parameter selected correlation function for the decay of $^7Be \rightarrow {}^3He + \alpha$ are shown in Figure 11. The left panel is gated on peripheral collisions and the right panel is gated on central collisions. The peak at $E_{rel} \approx 3$ MeV is from the decay of the ^7Be excited state at $E^* = 4.57$ MeV with spectroscopic information $J^\pi = \frac{7}{2}^-, \Gamma = 0.175$ MeV, $\Gamma_c/\Gamma = 1.0$. The peak is fitted with R-matrix formula with the relevant R-matrix parameters from refs. [23, 36, 38, 39]. At slightly higher energies, there are two peaks at $E^* = 6.73$ MeV, and $E^* = 7.21$ MeV. These two peaks are included in the fit with the two level R-matrix formula [23]. But the population probabilities for the pair of states were statistically insignificant and were not analyzed further. The energy spectra for stable ^7Be nuclei were used to calculate the efficiency functions. The population probabilities for the ^7Be excited

state at $E^* = 4.57$ in Table 2 are defined relative to the yield of stable ^7Be nuclei.

The impact parameter selected correlation functions for the decay of $^7Be \rightarrow p + {}^6Li$ are shown in Figure 12. The left panel is the data gated on peripheral collisions and the right panel is the data gated on central collisions. The peak at $E_{rel} \approx 1.6$ MeV is from the decay of the ^7Be excited state at $E^* = 7.21$ MeV with the spectroscopic parameters $J^\pi = \frac{5}{2}^-, \Gamma = 0.5$ MeV, $\Gamma_c/\Gamma = 0.97$. The Breit-Wigner formula is used to fit the energy spectrum and the extracted population probabilities are given in Table 2.

VI. The sequential decay calculations

While temperatures deduced from excited state populations are not affected by the collective motion of the colliding system, they are sensitive to sequential feeding from higher lying heavier particle unstable nuclei [40]. For example, ^{10}B particle unstable excited states can particle decay to ^{6}Li and α, ie, $^{10}B^* \rightarrow {}^6Li + \alpha$. Both ^{6}Li and α can be in a ground state or in an excited state. In this case, these daughter fragments, ^{6}Li and α, will increase the total populations of the respective ^{6}Li and α states, thus altering these populations from their initial values. Experimental measurements can not exclude these additional contributions from sequential feeding. Thus the experimentally measured temperature, derived from the population ratio of excited state yields to their ground state yields, is affected by the sequential feeding from such higher lying states . In this section, we will address this issue and discuss calculations to take this sequential feeding into account and make the corresponding corrections when extracting the temperature.

Following procedures outlined in ref. [23], we have estimated the corrections via sequential decay calculations. In this approach, the ensemble of emitted fragments is assumed to be described by local thermal equilibrium at a *freezeout* time after which all the fragments

cease to interact with each other. In this case, the yields of fragments and the detected populations of their excited states are dictated by the freezeout temperature as well as by the spins, parities, excitation energies of their low lying discrete states, level densities in the continuum and the binding energies. Taking these effects into consideration, the *primary populations* of excited states of emitted fragments can be obtained. These populations are subsequently altered by considering the sequential decay of the initial fragments using the formalism of Hauser and Feshbach [41].

For simplicity, the initial population of a particular excited state at excitation energy E* and spin J of a nucleus with mass number A and charge number Z can be written as

$$P_i(A, Z, E^*) \propto P_0(A, Z)\rho(E^*, J)exp(-E^*/T_{em}), \tag{13}$$

where $P_0(A, Z)$ is the probability of populating the nucleus with mass number A and charge number Z at its ground state. $\rho(E^*, J)$ is the density of levels of that nucleus with excitation energy E* and spin J. T_{em} is the emission temperature of the excited system [23, 40].

The population probability of ground state nuclei with charge number Z and mass number A can be parameterized by,

$$P_0(A, Z) \propto exp(-fV_c/T_{em} + Q/T_{em}). \tag{14}$$

The Coulomb barrier is parameterized by

$$V_c = \frac{Z(Z_p - Z)e^2}{r_0[A^{1/3} + (A_p - A)^{1/3}]}, \tag{15}$$

where A_p, Z_p are the total mass and charge number of the fragmenting system and $r_0 = 1.2$fm. Q is the separation energy calculated via the Weizacker formula [42]. The constant f is adjusted to provide an optimal agreement between the calculated final charge distribution and the measured charge distribution. Clearly, Equation 14 represents a simplification of the

emission mechanism. For example, in a real statistical model calculation, one has to consider the free energy besides the Coulomb energy and binding energy [30]. The adjustment of f could partially be regarded as a compensation for the neglect of such effects.

An important prerequisite for these calculations is that the observed elemental distributions for the fragments in their ground state are reproduced. Otherwise the calculation of sequential feeding corrections can be grossly incorrect. To achieve reasonable agreements between the calculated ground state populations and the experimental measurements, the constant f in Equation 14 which multiplies the Coulomb barrier was varied.

Figure 13 provides the corresponding charge distributions measured for the ^{36}Ar + ^{197}Au reaction at E/A=35 MeV. In order to reduce the effect of the detector threshold, a common threshold of E/A $>$ 5 MeV is used for all particles in this plot. Sequential decay calculations for the stable fragment yield at various initial temperatures are plotted as histograms. The optimal adjustment constants f for each temperature are given in the figure as well.

VII. Comparisons between calculated and measured population probabilities

Figure 14 shows the measured ^{10}B population probabilities (solid points) as a function of excitation energy for peripheral (left side) and central (right side) collisions [24]. The error bars include the uncertainties in the background subtraction bounded by the two assumed background coincidence yields displayed in Figure 7. In the absence of sequential feeding corrections, thermal models predict that the excited state population probabilities of intermediate mass fragments should be proportional to a Boltzmann factor, $exp(-E^*/T_{eff})$, where T_{eff} is the effective temperature of the system at breakup. The dashed lines in Figure 14 show the exponential dependence dictated by the Boltzmann factor for $T_{eff} = 4$

MeV. For peripheral collisions, the measured relative populations deviate significantly from the expected monotonic behavior and a population inversion is observed; the group of states at E $\approx$ 6.0 MeV is populated much more strongly than the lower lying states at 5.2 and 4.8 MeV. Such effects were also observed in the inclusive measurements of ref. [22]. The population inversion disappears for central collisions. The population probabilities, however, do not fall off exponentially as expected from the Boltzmann factor; instead, one observes an approximately constant population probability for the 5.2 and 6.0 MeV levels.

Recent shell model calculations [43] which reproduce many of the properties of ^{10}B excited states predict the existence of an additional $2\hbar\omega$ excited state near 6 MeV with $J^\pi = 3^+$. While the existence of this state has not been experimentally confirmed, we have estimated the effect on the population probability with this state included. The open points depict the experimental populations for the group of excited states at E* $\approx$ 6 MeV, assuming that this state adds to the experimentally observed peak with 100% branching ratio to the $\alpha + {}^6$Li channel. Taking this state into account lessens the population inversion for peripheral collisions and makes the population probabilities observed for central collisions decrease monotonically with excitation energy. This hypothetical 3^+ state was only included in the analysis for the construction of this figure. In subsequent figures and analyses, this state was not included because its existence has not, until now, been confirmed.

In order to provide an overall comparison between the calculated and measured population probabilities, a least squares analysis was performed by computing $\chi^2_\nu(T)$ for a range of initial emission temperatures.

$$\chi^2_\nu(T) = \frac{1}{\nu}\sum_{i=1}^{\nu}\frac{(n_{exp,i} - n_{cal,i}(T))^2}{\sigma^2_{exp,i} + \sigma^2_{cal,i}}. \tag{16}$$

Here, $n_{exp,i}$ and $n_{cal,i}(T)$ are the measured and calculated population probabilities and $\sigma^2_{exp,i}$ and $\sigma^2_{cal,i}$ are the corresponding uncertainties. The resulting values of $\chi^2(T)$ are shown in

Figure 15 as open points. The upper panel is for central collisions and the lower panel is for peripheral collisions. Optimal agreement between calculated and measured population probabilities is obtained for both central and peripheral collisions at temperatures of about $T \approx 3 - 5$ MeV. Similar residue temperatures have been obtained in dynamical [44, 45] and in statistical [31, 32, 33, 46] calculations.

For T = 4 MeV, the population probabilities obtained by the sequential decay calculations are indicated by the open bars in Figure 14; the vertical extent of the bars graphically demonstrates the range of theoretical values obtained for ten randomly chosen assumptions about the unknown spins and parities of excited states included in the calculation. Rotational effects were explored in ref. [23]. Those studies indicated that rotational effects may add uncertainties to the calculated population probabilities that are comparable to the above mentioned uncertainties due to incomplete spectroscopic information. Rotational effects cannot enhance the populations of the group of states at 6.0 MeV without similarly enhancing the populations of the state at 6.56 MeV. The lack of a comparable enhancement in the population of the state at 6.56 MeV therefore places a constraint upon the magnitude of possible rotational corrections to the extent that rotational effects cannot be the sole explanation for the observed enhancement of the group at 6.0 MeV. The population probabilities obtained from the sequential decay calculations cannot be reconciled with the population inversions observed for peripheral collisions. For central collisions, on the other hand, the discrepancies between calculated and measured population probabilities are much smaller, but still too large for a purely thermal interpretation. Inclusion of the predicted 3^+ state near $E^* = 6$ MeV, however, makes the data consistent with a thermal interpretation.

For a comparison between measured and calculated population probabilities for ^{5}Li, ^{6}Li and ^{7}Be nuclei, we take the following approach. In the absence of sequential feeding, the

ratio of the population probabilities of two levels should be given by,

$$\frac{n_1}{n_2} = e^{-(E_1^* - E_2^*)/T_{app}}. \tag{17}$$

where T_{app} is the apparent temperature at break up. In the event of large sequential decay corrections, using equation 17 to describe the experimental data has the consequence that T_{app} becomes an *apparent* temperature that can vary from state to state.

In Figure 16, we plot the compilation of extracted apparent temperatures of ^{5}Li, ^{6}Li and ^{7}Be nuclei with peripheral (lower) and central (upper) collision gates. The solid points are experimental measurements with the error bars mainly from the uncertainty of background subtraction. Using the sequential decay calculations, the same ratios of population probabilities can be calculated and a theoretical apparent temperature can be obtained. To illustrate the effects of sequential decay, the predictions of the sequential decay calculations for the apparent temperatures of an initial temperature T = 4 MeV are plotted as open points.(Note: this is not a fit.) The error bars for the calculations correspond to a range of calculated values for 12 calculations for different assumptions about the unknown spins and parities of excited states included in the calculation. Additional uncertainties in the calculated population probabilities due to the small observed impact parameter dependence of the elemental distributions [29] are smaller than the uncertainties associated with these spectroscopic uncertainties. Obviously, the apparent temperatures shown in Figure 16 are not all equal. The fluctuations in the predicted apparent temperatures are due to the sequential feeding of these states by the decays of heavier particle unstable fragments. To see what value of the initial temperature of the sequential decay calculation will best fit the overall measurement, we calculated the $\chi^2_\nu(T)$ defined by,

$$\chi^2_\nu(T) = \frac{1}{\nu}\sum_{i=1}^{\nu} \frac{(T_{exp,i} - T_{cal,i}(T))^2}{\sigma^2_{exp,i} + \sigma^2_{cal,i}}. \tag{18}$$

Here the summation is over the five measured apparent temperatures for ^{5}Li, ^{6}Li, and ^{7}Be nuclei. $T_{exp,i}$ is the apparent temperature calculated from the experimental data and shown as the solid points in Figure 16. Furthermore, T is the initial temperature of the sequential decay calculation and $T_{cal,i}(T)$ is the apparent temperature calculated in analogy to the experimental apparent temperature $T_{exp,i}$, using the final calculated population probabilities. Finally, $\sigma^2_{exp,i}$ is the experimental uncertainty, and $\sigma^2_{cal,i}$ is the theoretical uncertainty due to the unknown spin and parities. The solid squares in Figure 15 show the plot of $\chi^2(T)$ from Equation 18 as a function of T, the initial freezeout temperature assumed in the sequential decay calculations. The upper panel is for central collision gate and the lower panel is for peripheral collision gate. The $\chi^2(T)$ has its minimum between 4-5 MeV for central collision gate. The minimum for peripheral collision gate is at 3-4 MeV. The minimum of $\chi^2(T)$ function for central collision gate is smaller than that for peripheral collision gate, meaning that the measured data from central collisions deviates less from an initially equilibrated system than that from peripheral collisions. A greater degree of equilibration for central collisions is in agreement with the conclusions derived from the excited states of ^{10}B nuclei discussed in this section.

Figure 15 summarizes both χ^2_ν analyses for ^{10}B excited states (open circles) and for $^{5,6}Li$ and ^7Be excited states (solid squares). For central collisions, both χ^2_ν analyses yield minima for $T \approx 4-5$ MeV. The overall value for χ^2_ν are close to one, indicating that the experimental and theoretical excited state populations are close to being in statistical agreement. In contrast, the minimum for ^{10}B excited state populations in peripheral collisions occurs at $T \approx 5$ MeV; for $^{5,6}Li$ and ^7Be excited states, the minimum occurs at 3-4 MeV. The overall χ^2_ν for peripheral collisions are rather large, indicating a significant disagreement between theoretical and experimental population probabilities. Thus the additional information provided by the ^{5,6}Li and ^{7}Be excited state populations provides a strong confirmation of

the observations of non-statistical populations for peripheral collisions and nearly statistical populations for central collisions derived from the ^{10}B excited states.

VIII. Summary

To summarize, the impact parameter dependence of excited state populations of intermediate mass fragments has been investigated with a high resolution hodoscope and a 4π charged particle array. Non-statistical populations, indicative of non-thermal excitation mechanisms, are observed in peripheral collisions characterized by low associated charged particle multiplicities. These effects largely disappear for central collisions, consistent with a trend towards greater thermalization as the complexity of the breakup configuration is increased. The remaining discrepancies observed in central collisions, however, indicate that the limit of local equilibrium has not yet been observed. If one includes a predicted ^{10}B 3^+ state at $E^* \approx 6$ MeV, which has not been observed experimentally so far, the data for central collisions become consistent with the statistical equilibrium distribution. However, for peripheral collisions, calculated and measured populations remain in disagreement.

ACKNOWLEDGMENTS

This manuscript is based upon work supported by the National Science Foundation under Grant number PHY-89-13815. W.G. Lynch acknowledges the receipt of a U.S. Presidential Young Investigator Award. The authors thank the contributions from J. Dinius, Dr. T. Murakami and Dr. T. Nayak for the early preparation of this experiment and Dr. B.A. Brown for suggesting the ^{10}B 3^+ state.

References

a. Present address: Physics Department, Brookhaven National Laboratory, Upton, NY 11973

b. Present address: Chalk River Laboratories, Chalk River, K0J 1J0, Canada

c. Present address: Department of Chemistry and Indiana University Cyclotron Facility, Bloomington, IN 47405

d. Present address: National Laboratory for High Energy Physics (KEK), 1-1 Oho, Tsukuba, Ibaraki 305, Japan

e. Nuclear Science Division, Lawrence Berkeley Laboratory, Berkeley, CA 94720

f. Present address: Cyclotron Institute, Taxas A&M University,

[1] C.K. Gelbke, and D.H. Boal, Prog. Part. and Nucl. Phys. **19** (1987) 33, and references contained therein.

[2] E. Suraud, C. Grégoire, and B. Tamain, Prog. Part. Nucl. Phys. **23** (1989) 357, and references contained therein.

[3] D. Guerreau, "Nuclear Matter and Heavy Ion Collisions", Plenum Press, Nato ASI Series B 205 (1989) 187, and references contained therein.

[4] L.P. Csernai, and J.I. Kapusta, Phys. Rep. **131** (1986) 223, and references contained therein.

[5] W.G. Lynch, Ann. Rev. Nucl. Part. Sci. **37** (1987) 493, and references contained therein.

[6] R.T. de Souza, L. Phair, D.R. Bowman, N. Carlin, C.K. Gelbke, W.G. Gong, Y.D. Kim, M.A. Lisa, W.G. Lynch, G.F. Peaslee, M.B. Tsang, H.M. Xu, and F. Zhu, Phys. Lett. **B268** (1991) 6.

[7] D.R. Bowman, G.F. Peaslee, R.T. de Souza, N.Carlin, C.K. Gelbke, W.G. Gong, Y.D. Kim, M.A. Lisa, W.G. Lynch, L. Phair, M.B. Tsang, C. Williams, Phys. Rev. Lett. **67** (1991) 1527.

[8] C.A. Ogilvie, J.C. Adloff, M. Begemann-Blaich, P. Bouissou, J. Hubele, G. Imme, I. Iori, P. Kreutz, G.J. Kunde, S. Leray, V. Lindenstruth, Z. Liu, U. Lynen, R.J. Meijer, U. Milkau, W.F.J. Müller, C. Ngô, J. Pochodzalla, G. Raciti, G. Rudolf, H. Sann, A. Schüttauf, W. Seidel, L. Stuttge, W. Trautmann, and A. Tucholski, Phys. Rev. Lett. **67** (1991) 1214.

[9] D. Morrisey, W. Benenson and W.A. Friedman, Ann. Rev. Nucl. Part. Sci. **45** in press.

[10] J. Gomez del Campo, J.L. Chavet, A. D'Onofrio, R.L. Auble, J.R. Beene, M.L. Halbert, and H.J. Kim, Phys. Rev. Lett. **61** (1988) 290.

[11] D.J. Morrissey, C. Bloch, W. Benenson, E. Kashy, R.A. Blue, R.M. Ronningen, and R. Aryaeinejad, Phys. Rev. **C34** (1986) 761.

[12] J. Lee, W. Benenson, and D.J. Morrissey, Phys. Rev. **C41** (1990) 1562.

[13] J. Lee, W. Benenson, C. Bloch, Y. Chen, R.J. Radtke, E. Kashy, M.F. Mohar, D.J. Morrissey, R. Blue, and R. Ronningen, Phys. Rev. **C41** (1990) 2406.

[14] S.J. Sanders, B.B. Back, R.V.F. Janssens, D.G. Kovar, D. Habs, D. Henderson, T.-L. Khoo, H. Korner, G-E. Rathke, T.F. Wang, F.L.H. Wolfs, and K.B. Beard, Phys. Rev. **C41** (1990) R1901.

[15] D.J. Morrissey, W. Benenson, E. Kashy, B. Sherrill, A.D. Panagiotou, R.A. Blue, R.M. Ronningen, J. van der Plicht, and H. Utsunomiya, Phys. Lett. **B148** (1984) 423.

[16] J. Pochodzalla, W.A. Friedman, C.K. Gelbke, W.G. Lynch, M.R. Maier, D. Ardouin, H. Delagrange, H. Doubre, C. Grégoire, A. Kyanowski, W. Mittig, A. Péghaire, J. Péter, F. Saint-Laurent, Y.P. Viyogi, B. Zwieglinski, G. Bizard, F. Lefèbvres, B. Tamain, and J. Québert, Phys. Rev. Lett. **55** (1985) 177.

[17] J. Pochodzalla, C.K. Gelbke, W.G. Lynch, M.R. Maier, D. Ardouin, H. Delagrange, H. Doubre, C. Grégoire, A. Kyanowski, W. Mittig, A. Péghaire, J. Péter, F. Saint-Laurent, B. Zwieglinski, G. Bizard, F. Lefèbvres, B. Tamain, and J. Québert, Y.P. Viyogi, W.A. Friedman, and D.H. Boal, Phys. Rev. **C35**, 1695(1987).

[18] H.M. Xu, W.G. Lynch, C.K. Gelbke, M.B. Tsang, D.J. Fields, M.R. Maier, D.J. Morrissey, J. Pochodzalla, D.G. Sarantites, L.G. Sobotka, M.L. Halbert, D.C. Hensley, D. Hahn, and H. Stöcker, Phys. Lett. **B182** (1986) 155.

[19] Z. Chen, C.K. Gelbke, W.G. Gong, Y.D. Kim, W.G. Lynch, M.R. Maier, J. Pochodzalla, M.B. Tsang, F. Saint-Laurent, D. Ardouin, H. Delagrange, H. Doubre, J. Kassagi, A. Kyanowski, A. Péghaire, J. Péter, E. Rosato, G. Bizard, F. Lefèbvres, B. Tamain, J. Québert, and Y.P. Viyogi, Phys. Lett. **B199** (1987) 171.

[20] G.J. Kunde, J. Pochodzalla, J. Aichelin, E. Berdermann, B. Berthier, C. Cerruti, C.K. Gelbke, J. Hubele, P. Kreutz, S. Leray, R. Lucas, U, Lynen, U. Milkau, W.F.J. Müller, C. Ngô, C.H. Pinkenburg, G. Raciti, H. Sann and W. Trautmann, Phys. Lett. **B272** (1991) 202.

[21] C. Schwarz, W.G. Gong, N. Carlin, C.K. Gelbke, Y.D. Kim, W.G. Lynch, T. Murakami, G. Poggi, R.T. de Souza, M.B. Tsang, H.M. Xu, D.E. Fields, K. Kwiatkowski, V.E. Viola,Jr., and S.J. Yennello, Phys. Rev. **C48** 676 (1993).

[22] T.K. Nayak, T. Murakami, W.G. Lynch, K. Swartz, D.J. Fields, C.K. Gelbke, Y.D. Kim, J. Pochodzalla, M.B. Tsang, H.M. Xu, F. Zhu, and K. Kwiatkowski, Phys. Rev. Lett. **62** (1989) 1021.

[23] T.K. Nayak, T. Murakami, W.G. Lynch, K. Swartz, D.J. Fields, C.K. Gelbke, Y.D. Kim, J. Pochodzalla, M.B. Tsang, H.M. Xu, F. Zhu, and K. Kwiatkowski, Phys. Rev. C, **C45**, (1992) 132.

[24] F. Zhu, W.G. Lynch, D.R. Bowman, R.T. de Souza, C.K. Gelbke, Y.D. Kim, L. Phair, M.B. Tsang, C. Williams, H.M. Xu, and J. Dinius, Phys. Lett. **B282** (1992) 299

[25] T.C. Awes, R.L. Ferguson, R. Novotny, F.E. Obenshain, F. Plasil, S. Pontoppidan, V. Rauch, G.R. Young, and H. Sann, Phys. Rev. Lett. 52 (1984) 251.

[26] T. Døssing and J. Randrup, Nucl. Phys. **A433** (1985) 215; **A433** (1985) 280.

[27] J. Randrup, Nucl. Phys. **A307** (1978) 319; **A327** (1979) 490.

[28] R. Vandenbosch, A. Lazzarini, D. Leach, D.-K. Lock, A. Ray, and A. Seamster, Phys. Rev. Lett. **52** (1984) 1964.

[29] Y.D. Kim, R.T. de Souza, D.R. Bowman, N. Carlin, C.K. Gelbke, W.G. Gong, W.G. Lynch, L. Phair, M.B. Tsang, and F. Zhu, Phys. Rev. **C45** (1992) 338.

[30] W.A. Friedman and W.G. Lynch, Phys. Rev. **C28** (1983) 16.

[31] W.A. Friedman, Phys. Rev. Lett. **60** (1988) 2125

[32] D.H.E. Gross, Phys. Lett. **B203** (1988) 26.

[33] J.P. Bondorf, R. Donangelo, L.N. Mishustin, C.J. Pethick, H.Schulz, and K. Sneppen, Nucl. Phys. **A443** (1985) 321.

[34] T. Murakami, T.K. Nayak, W.G. Lynch, K. Swartz, Z. Chen, D.J. Fields, C.K. Gelbke, Y.D. Kim, M.R. Maier, J. Pochodzalla, M.B. Tsang, H.M. Xu, and F. Zhu, Nucl. Instr. and Meth. **A275** (1989) 112.

[35] R.T. de Souza, N. Carlin, Y.D. Kim, J. Ottarson, L. Phair, D.R. Bowman, C.K. Gelbke, W.G. Gong, W.G. Lynch, R.A. Pelak, T. Peterson, G. Poggi, M.B. Tsang, and H.M. Xu, Nucl. Instr. and Meth. **A295** (1990) 109.

[36] F. Ajzenberg-Selove, Nucl. Phys. **A475** (1987) 1; **A413** (1984) 1; **A433** (1985) 1; **A449** (1986) 1; **A460** (1986) 1.

[37] J. Pochodzalla, C.B. Chitwood, D.J. Fields, C.K. Gelbke, W.G. Lynch, M.B. Tsang, D.H. Boal, and J.C. Shillcock, Phys. Lett. **B174**, 36 (1986).

[38] R.J. Spiger, and T.A. Tombrello, Phys. Rev. **163** (1967) 964.

[39] F.C. Barker, Aust. J. Phys. **25** (1972) 341.

[40] Z. Chen and C.K. Gelbke, Phys. Rev. C38, 2630(1988).

[41] W. Hauser and H. Feshbach, Phys. Rev. **87** (1952) 366.

[42] P. Marmier and E. Shelton, Physics of Nuclei and Particles, Vol. 1, Academic Press (1969) 38.

[43] E.K. Warburton and B.A. Brown, Phys. Rev. **C46** (1992) 923.

[44] H.M. Xu, P. Danielewicz, and W.G. Lynch, Phy. Lett. **B299** 199(1992)

[45] D. Boal, J. Glosli, and C. Wicentowich, Phys. Rev. **C40** (1989) 601.

[46] S. Levit and P. Bonche, Nucl. Phys. **A437** (1984) 426.

Figure Captions

Fig 1: The plot shows the total charged particle multiplicity distribution (upper panel) and the extracted impact parameter (lower panel) and their relationship, from ^{36}Ar + ^{197}Au reaction at E/A = 35 MeV with Miniball as a stand-alone device [29].

Fig 2: The cross calibration of the associated and the total multiplicities and the extracted impact parameter for the ^{36}Ar + ^{197}Au reaction at E/A = 35MeV.

Fig 3: The inclusive associated multiplicity distribution, arbitrarily normalized, of the Miniball array is shown as a dashed line for the ^{36}Ar + ^{197}Au reaction at E/A = 35MeV. The solid squares and open circles depict the distribution when ^{10}B nuclei or protons are detected in the hodoscope, respectively. The solid circles represents the distribution obtained by requiring α and ^{6}Li detected in coincidence in the hodoscope.

Fig 4: Energy spectra for ^{10}B nuclei detected at 45^0 in the high resolution hodoscope, for low multiplicity (solid points) and high multiplicity (solid squares) gates on the Miniball. The solid lines show moving source fits, used in the efficiency calculations.

Fig 5: Single particle cross sections for ^{4}He, ^{6}Li and ^{7}Be particles emitted in the ^{36}Ar + ^{197}Au reaction at E/A=35 MeV. The left and right panels show the results for peripheral ($N_A \leq 5$) and central ($N_A \geq 10$) collision gate, respectively. The curves show the moving source fits using Equation 2 with fitting parameters shown in table 1.

Fig 6: The efficiency function and energy resolution calculations of detecting ^{10}B nuclei excited states in the ^{36}Ar + ^{197}Au reaction at E/A = 35 MeV.

Fig 7: Yields for the decays: $^{10}B \rightarrow {}^{6}Li + \alpha$ (upper half) and $^{10}B \rightarrow {}^{9}Be + p$ (lower half). Spectra obtained for peripheral and central collisions are shown on the left and right hand sides, respectively. The curves are described in the text.

Fig 8: The $p-\alpha$ correlation function measured in the ^{36}Ar + ^{197}Au reaction at E/A=35 MeV. The spectra obtained for peripheral and central collisions are shown on the left and right hand sides, respectively. The curves are described in the text.

Fig 9: The $d-$ ^{3}He correlation function measured in the ^{36}Ar + ^{197}Au reaction at E/A=35 MeV. The spectra obtained for peripheral and central collisions are shown on the left and right hand sides, respectively. The curves are described in the text.

Fig 10: The correlation function of $d-\alpha$ measured in the ^{36}Ar + ^{197}Au reaction at E/A=35 MeV. The spectra obtained for peripheral and central collisions are shown on the left and right hand sides, respectively. The curves are described in the text.

Fig 11: The $^{3}He-\alpha$ correlation function measured for the ^{36}Ar + ^{197}Au reaction at E/A=35 MeV. The spectra obtained for peripheral and central collisions are shown on the left and right hand sides, respectively. The curves are described in the text.

Fig 12: The $p-$ ^{6}Li correlation function measured for the ^{36}Ar + ^{197}Au reaction at E/A=35 MeV. The spectra obtained for peripheral and central collisions are shown on the left and right hand sides, respectively. The curves are described in the text.

Fig 13: The charged particle yield distribution compared with the sequential decay calculations for ^{36}Ar + ^{197}Au reactions at E/A=35 MeV.

Fig 14: The solid points designate population probabilities for the excited states of ^{10}B nuclei measured for peripheral (left side) and central (right side) collisions. The open bars indicate the results of the sequential decay calculations. The dashed lines denote exponential exp(-E/T) with T = 4 MeV.

Fig 15: The open points are $\chi^2(T)$ values as a function of T calculated from Equation 16 for ^{10}B excited states; the solid squares are $\chi^2(T)$ values as a function of T calculated

from Equation 18 for ^{5,6}Li, and ^{7}Be excited states in the reaction of ^{36}Ar + ^{197}Au at E/A=35 MeV. The upper panel is for central collision gate and the lower panel is for peripheral collision gate, respectively. The lines are drawn to guide the eye.

Fig 16: The compilation of extracted *apparent* temperatures of ^{5,6}Li, and ^{7}Be nuclei in the reactions of ^{36}Ar + ^{197}Au at E/A=35 MeV with peripheral(lower) and central(upper) collisions gate. The solid points are experimental measurements and the open points are the results of sequential decay calculation for an initial temperature of T = 4 MeV.

Table 1: The moving source fitting parameters of the energy spectrum of peripheral collision gate (top panel) and central collision gate (bottom panel) for particles produced in ^{36}Ar + ^{197}Au reactions at E/A=35MeV. The cross section unit for N_i is $\mu b/(sr \cdot MeV^{3/2})$, the temperature unit for T_i is MeV.

Part	N_1	β_1	T_1	N_2	β_2	T_2	N_3	β_3	T_3
^{4}He	2942	0.0155	2.81	1875	0.0575	7.43	1248	0.1588	12.34
^{6}Li	417.5	0.0001	13.52	622.7	0.1393	15.12			
^{7}Be	111.8	0.0435	3.42	90.22	0.1056	19.20	1534	0.2085	9.27
^{10}B	41.99	0.0543	14.74	89.25	0.1346	17.98			

^{4}He	1920	0.0001	10.72	1351	0.0814	6.14	471.8	0.1478	10.68
^{6}Li	403.1	0.0790	14.00	931.2	0.1870	8.34			
^{7}Be	14.19	0.0001	26.21	53.05	0.0826	15.88	170.8	0.1759	9.52
^{10}B	78.28	0.086	13.67	46.77	0.1595	11.40			

Table 2: Spectroscopic information for $^{5,6}Li$, ^{7}Be, and ^{10}B isotopes that was used to extract excited state populations. Branching ratios are given in percentage. The group structure and population probabilities n_λ are explained in the text. The $n_\lambda(P)$ are for peripheral collisions and the $n_\lambda(C)$ are for central collisions.

	G	E*(MeV)	J^π	Γ_c(MeV)	Decay	Γ_c/Γ	$n_\lambda(P)$	$n_\lambda(C)$
^{5}Li	1	g.s	$\frac{3}{2}^-$	1.5	$\alpha - p$	100	0.325 ± 0.041	0.212 ± 0.085
	2	16.66	$\frac{3}{2}^+$	0.20	$^3He - d$	86	$(6.25 \pm 2.55) \times 10^{-3}$	$(3.93 \pm 3.77) \times 10^{-3}$
^{6}Li	1	2.186	3^+	0.024	$\alpha - d$	100	0.173 ± 0.0044	0.152 ± 0.0063
^{7}Be	1	4.57	$\frac{7}{2}^-$	0.175	$^3He - \alpha$	100	0.0497 ± 0.0016	0.0364 ± 0.0011
	2	7.21	$\frac{5}{2}^-$	0.5	$^6Li - p$	97	0.0134 ± 0.0042	0.0237 ± 0.0028

	G	E*(MeV)	J^π	Γ_c(KeV)	Decay	Γ_c/Γ	$n_\lambda(P)$	$n_\lambda(C)$
^{10}B	1	4.774	3^+	0.0084	$^6Li - \alpha$	100	$(14.4 \pm 0.66) \times 10^{-3}$	$(14.8 \pm 1.1) \times 10^{-3}$
	2	5.1103	2^-	0.98	$^6Li - \alpha$	100	$(12.2 \pm 0.66) \times 10^{-3}$	$(13.2 \pm 1.1) \times 10^{-3}$
		5.1639	2^+	0.00176	$^6Li - \alpha$	13		
		5.180	1^+	110	$^6Li - \alpha$	100		
	3	5.9195	2^+	6	$^6Li - \alpha$	100	$(17.7 \pm 1.1) \times 10^{-3}$	$(13.3 \pm 0.99) \times 10^{-3}$
		6.0250	4^+	0.05	$^6Li - \alpha$	100		
		6.1272	3^-	2.36	$^6Li - \alpha$	97		
	4	6.56	4^-	25.1	$^6Li - \alpha$	100	$(9.24 \pm 1.2) \times 10^{-3}$	$(8.14 \pm 1.21) \times 10^{-3}$
	5	7.430	2^-	100	$^9Be - p$	70	$(7.26 \pm 0.96) \times 10^{-3}$	$(6.93 \pm 0.99) \times 10^{-3}$
		7.467	1^+	65	$^9Be - p$	100		
		7.478	2^+	74	$^9Be - p$	65		
		7.5599	0^+	2.65	$^9Be - p$	100		

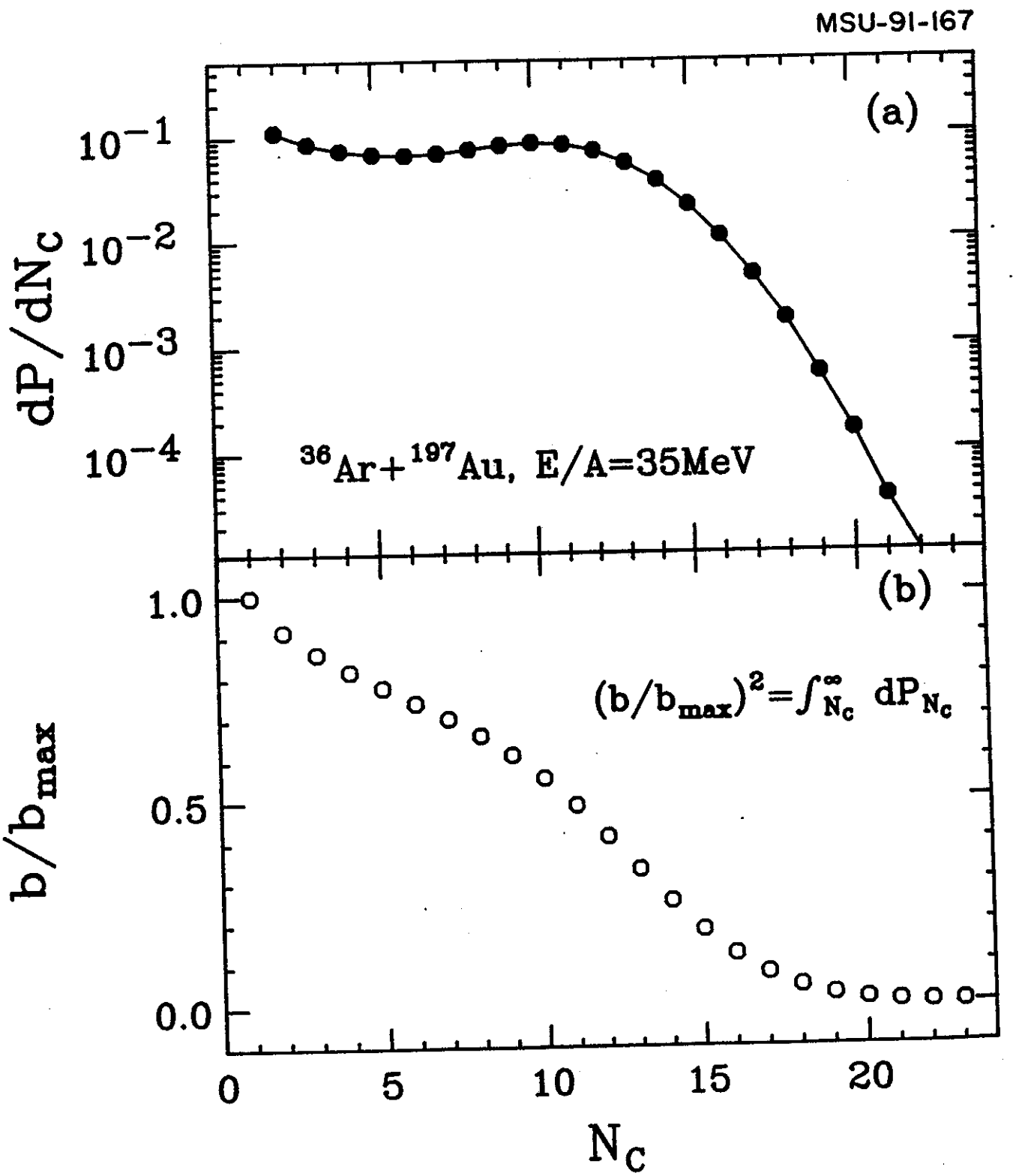
MSU-91-167
(a)
10^{-1}
10^{-2}
10^{-3}
10^{-4}
dP/dN$_c$
^{36}Ar+^{197}Au, E/A=35MeV
(b)
1.0
0.5
0.0
b/b$_{max}$
$(b/b_{max})^2=\int_{N_c}^{\infty} dP_{N_c}$
0
5
10
15
20
N$_c$

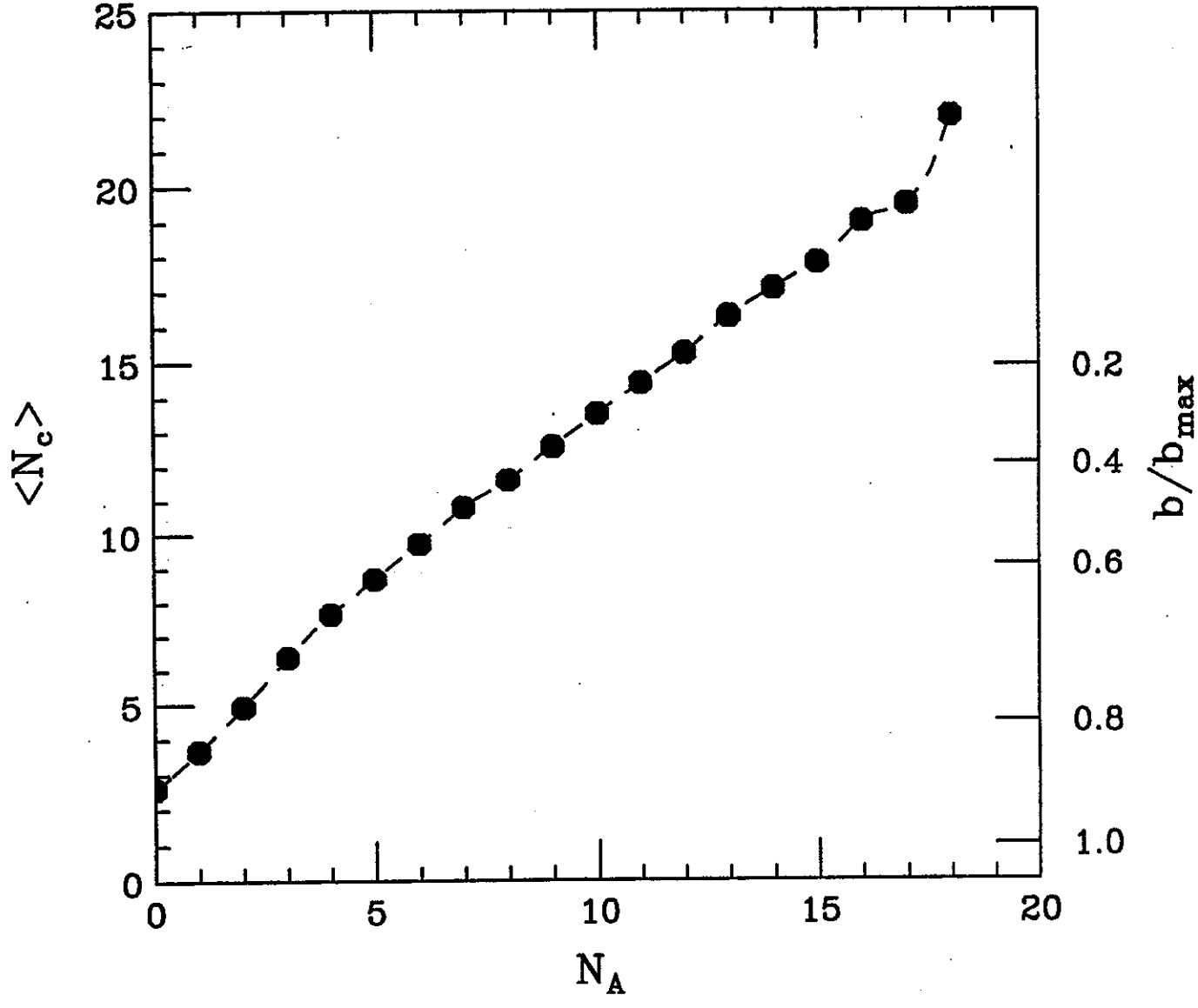
25
20
15
10
5
0
0
5
10
15
20
N_A
$\langle N_c \rangle$
0.2
0.4
0.6
0.8
1.0
b/b_{max}

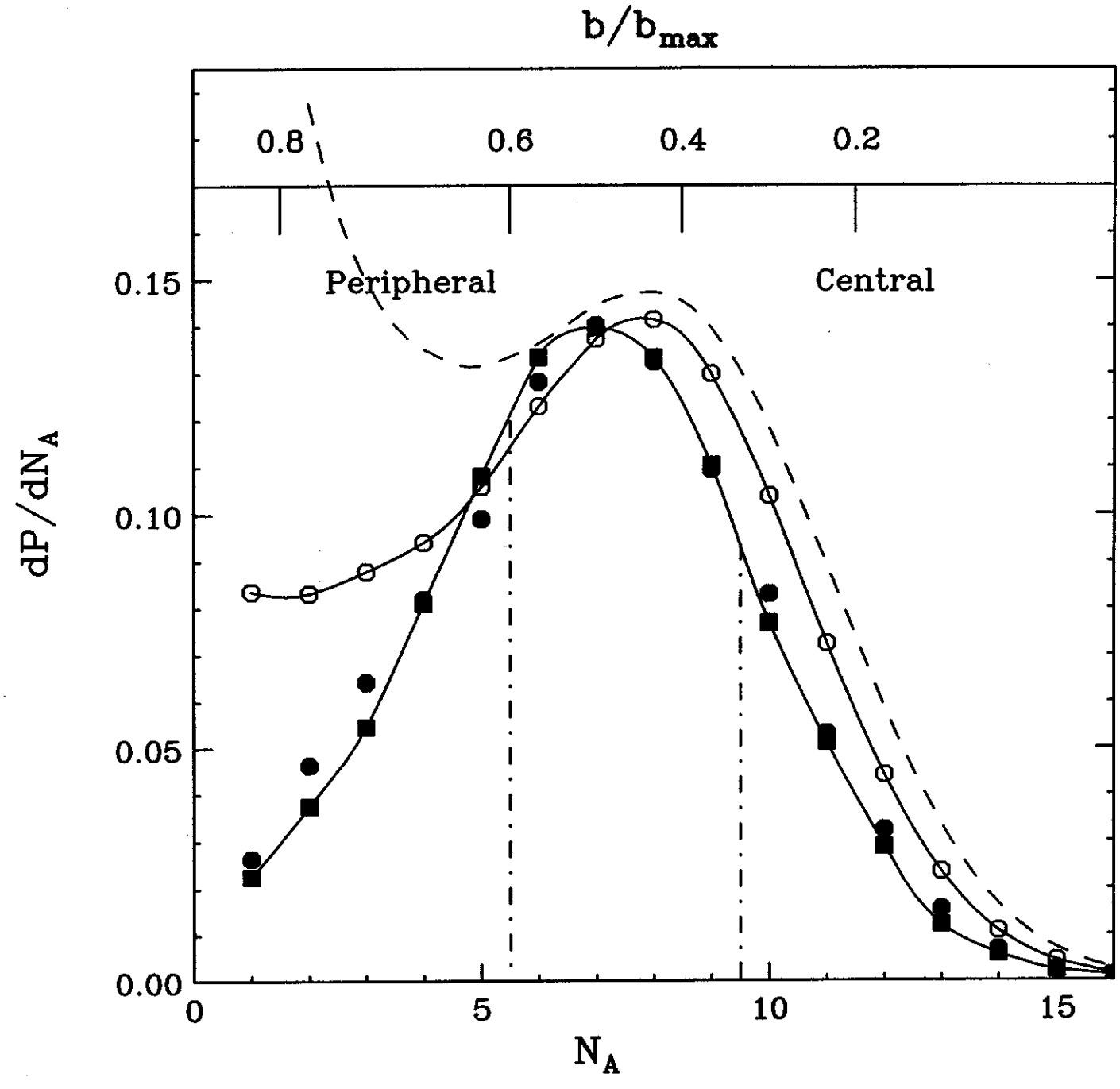
b/b_max
0.8
0.6
0.4
0.2
Peripheral
Central
dP/dN_A
0.15
0.10
0.05
0.00
0
5
10
15
N_A

fig 3

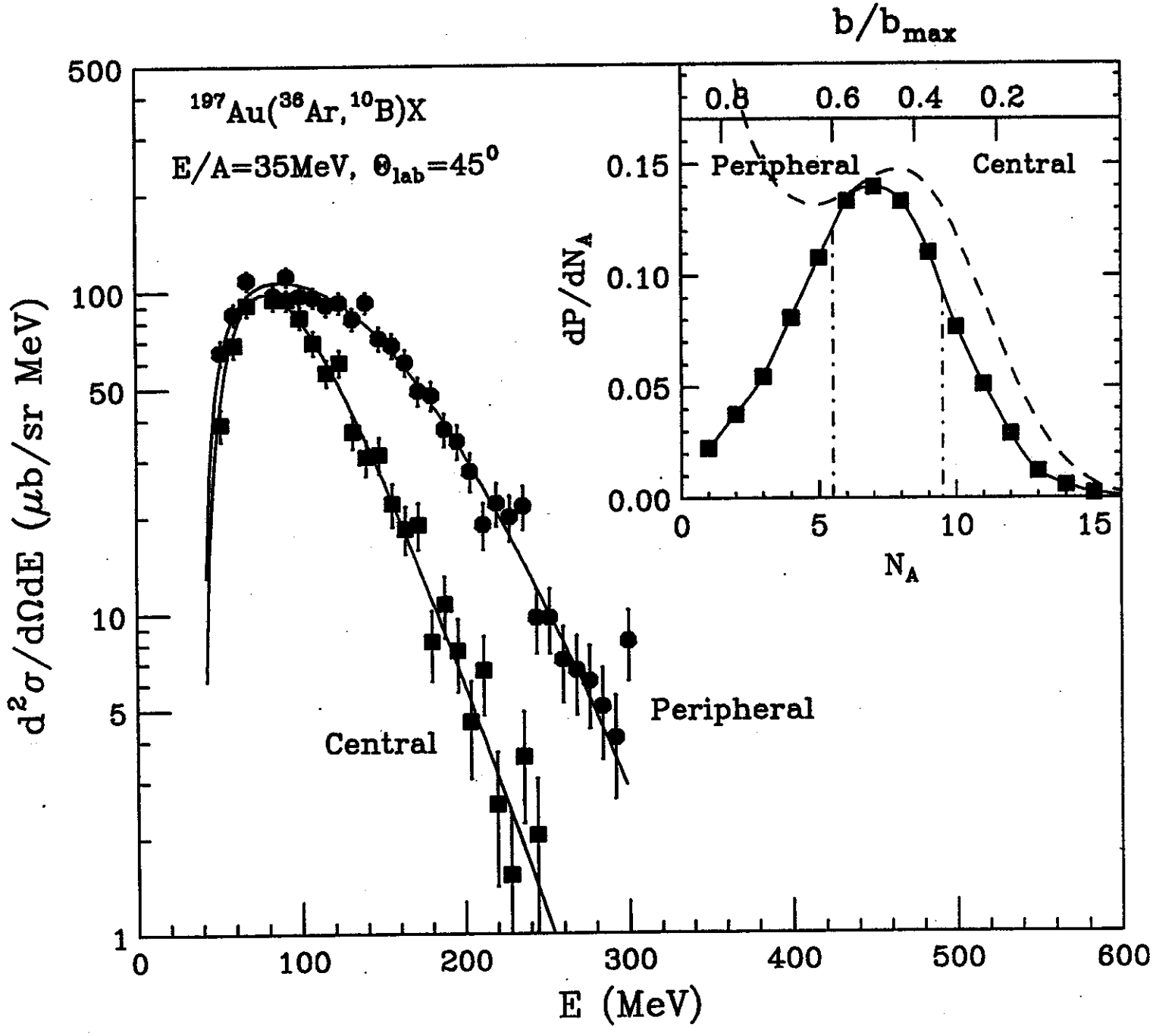
^{197}Au(^{36}Ar,^{10}B)X
E/A=35MeV, θ_{lab}=45^0
$d^2\sigma/d\Omega dE$ (μb/sr MeV)
E (MeV)
Central
Peripheral
b/b_{max}
0.8
0.6
0.4
0.2
Peripheral
Central
dP/dN$_A$
N$_A$

fig 4

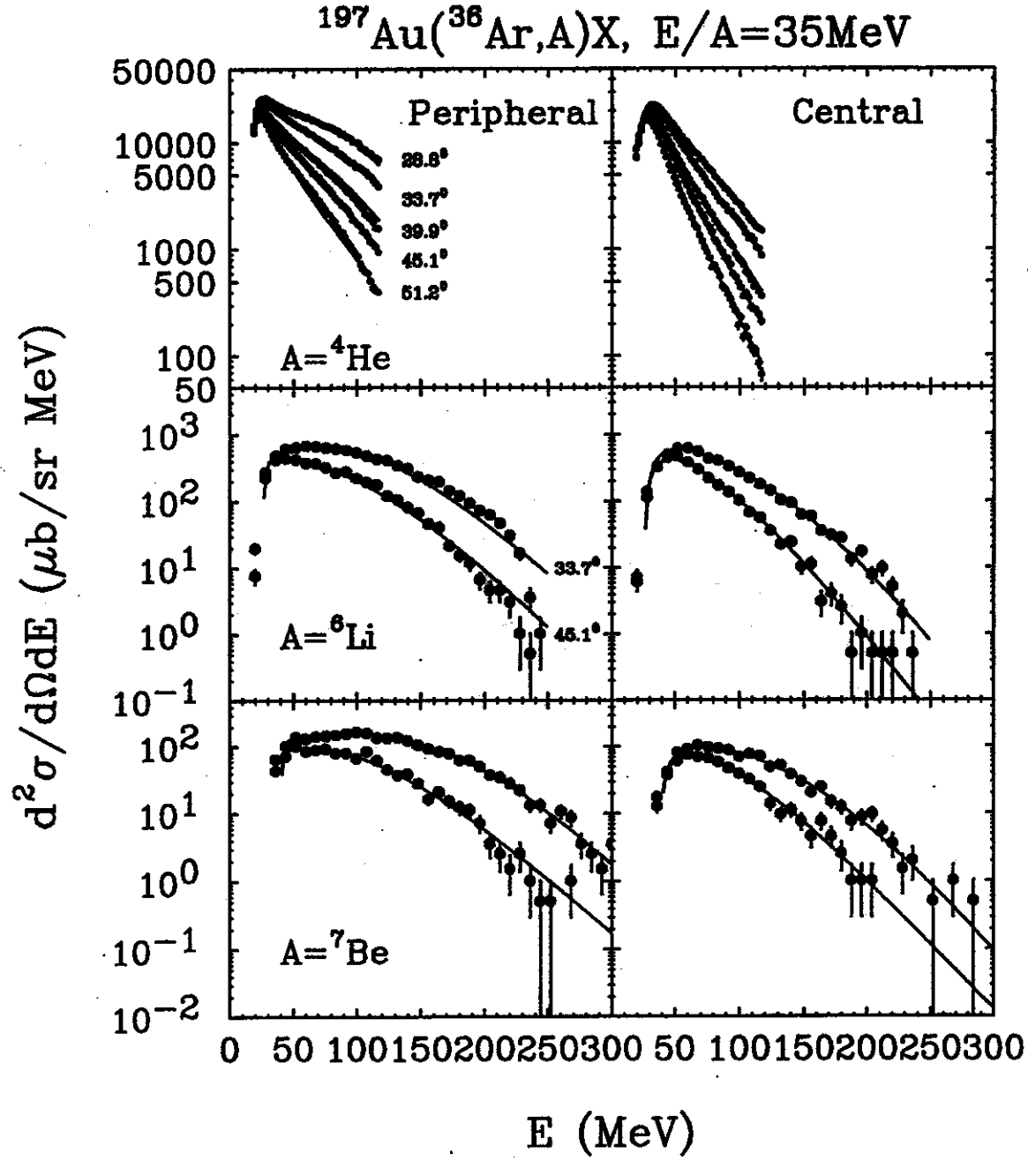
^{197}Au(^{36}Ar,A)X, E/A=35MeV
Peripheral
Central
28.6°
33.7°
39.9°
45.1°
51.2°
A=^{4}He
A=^{6}Li
A=^{7}Be
33.7°
45.1°
$d^2\sigma/d\Omega dE$ (μb/sr MeV)
E (MeV)

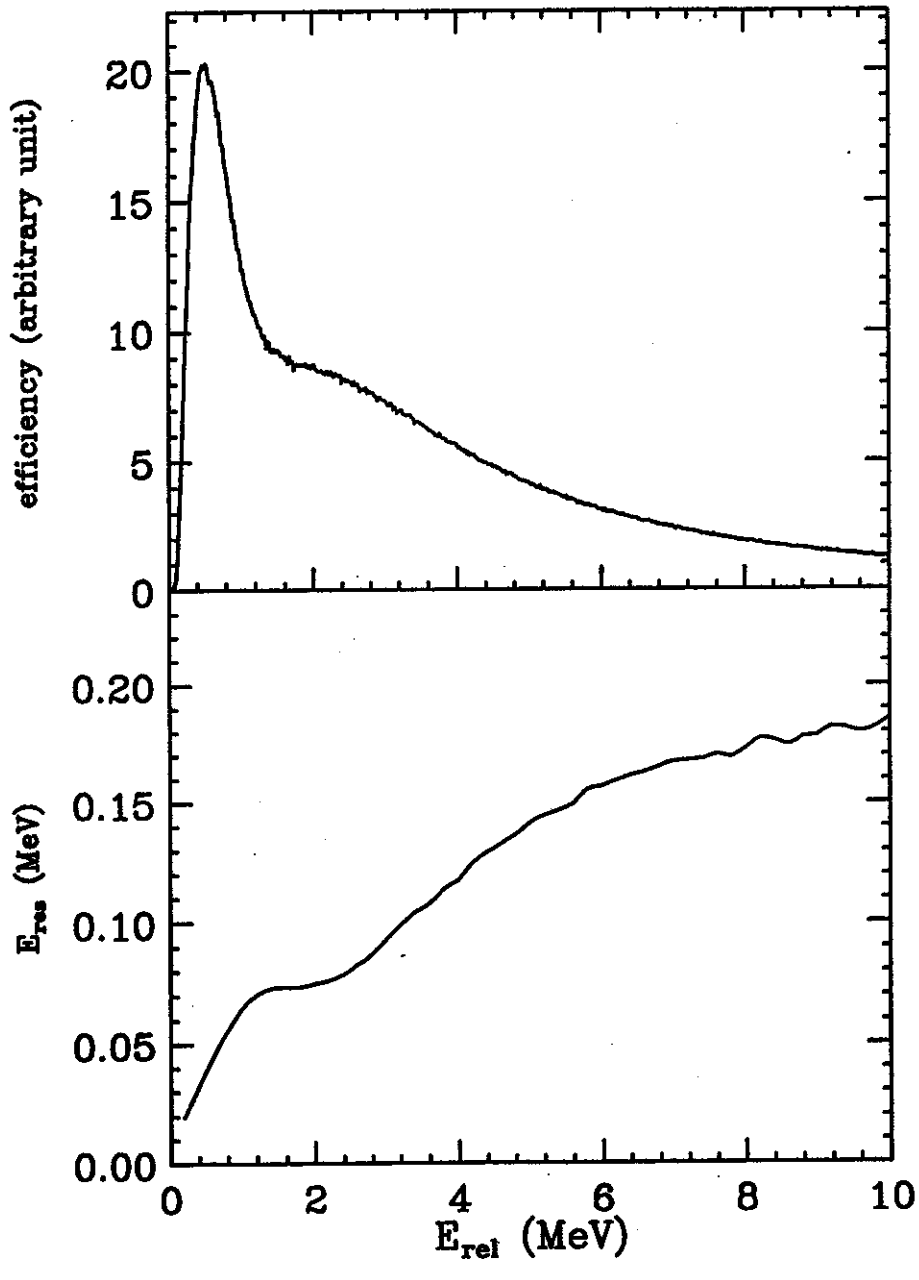
efficiency (arbitrary unit)
20
15
10
5
0
0.20
0.15
0.10
0.05
0.00
E_{res} (MeV)
0
2
4
6
8
10
E_{rel} (MeV)

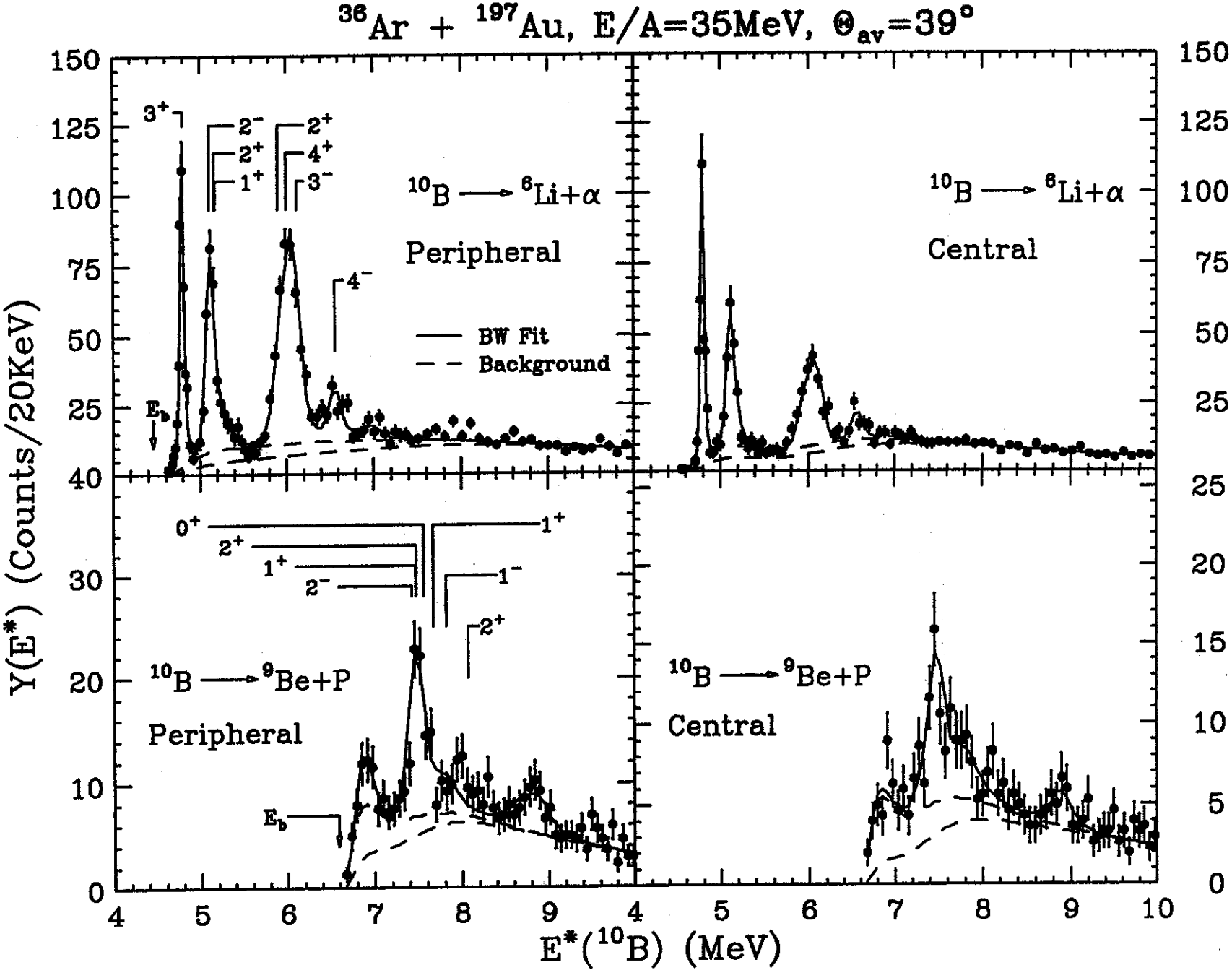
$^{36}Ar + {}^{197}Au$, E/A=35MeV, Θ_{av}=39°
$^{10}B \longrightarrow {}^{6}Li+\alpha$
Peripheral
Central
BW Fit
Background
3^+
2^-
2^+
1^+
2^+
4^+
3^-
4^-
E_b
$^{10}B \longrightarrow {}^{9}Be+P$
0^+
2^+
1^+
2^-
1^+
1^-
2^+
Y(E*) (Counts/20KeV)
E*(^{10}B) (MeV)

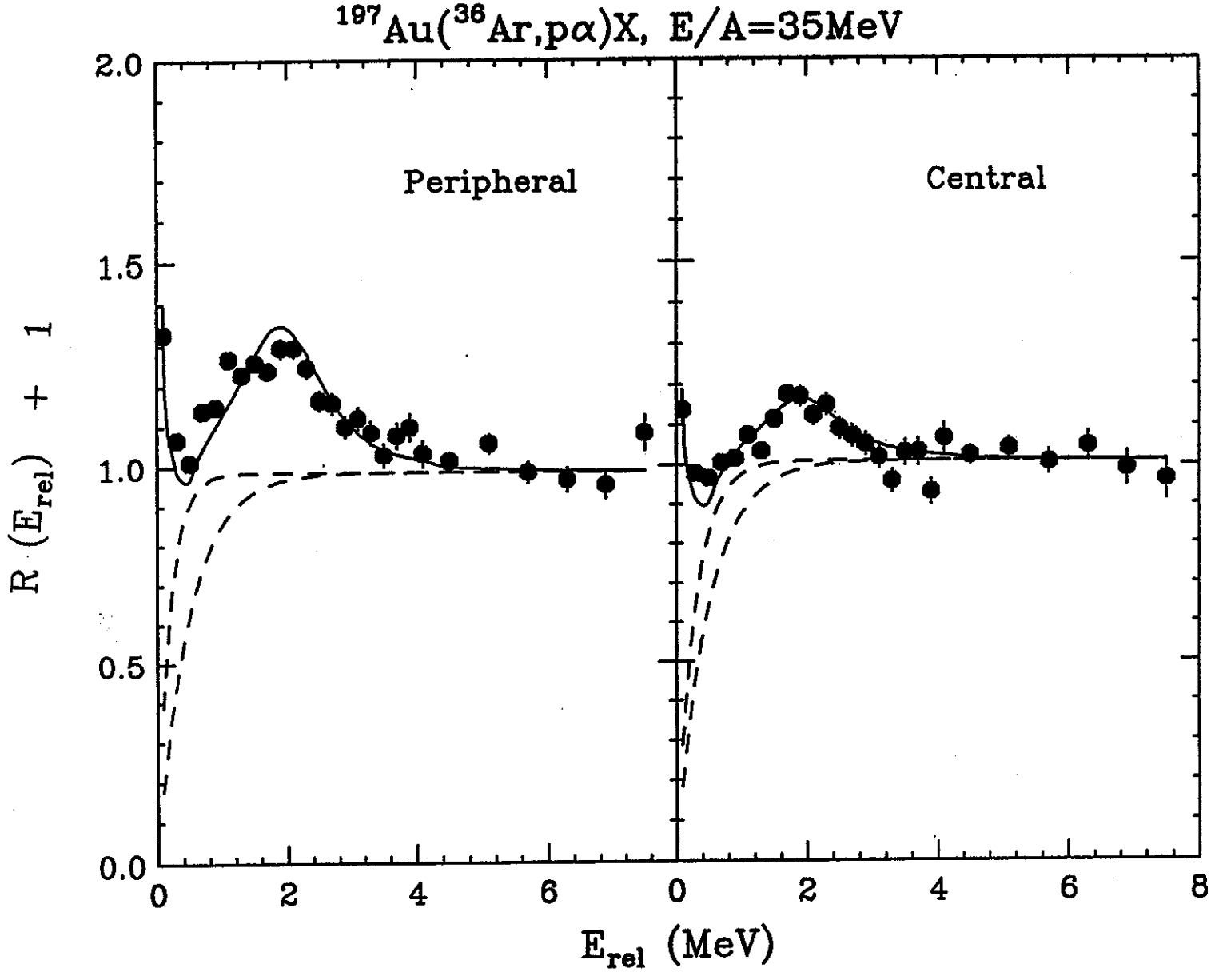
^{197}Au(^{36}Ar,pα)X, E/A=35MeV
Peripheral
Central
R (E_{rel}) + 1
E_{rel} (MeV)
2.0
1.5
1.0
0.5
0.0
0
2
4
6
0
2
4
6
8

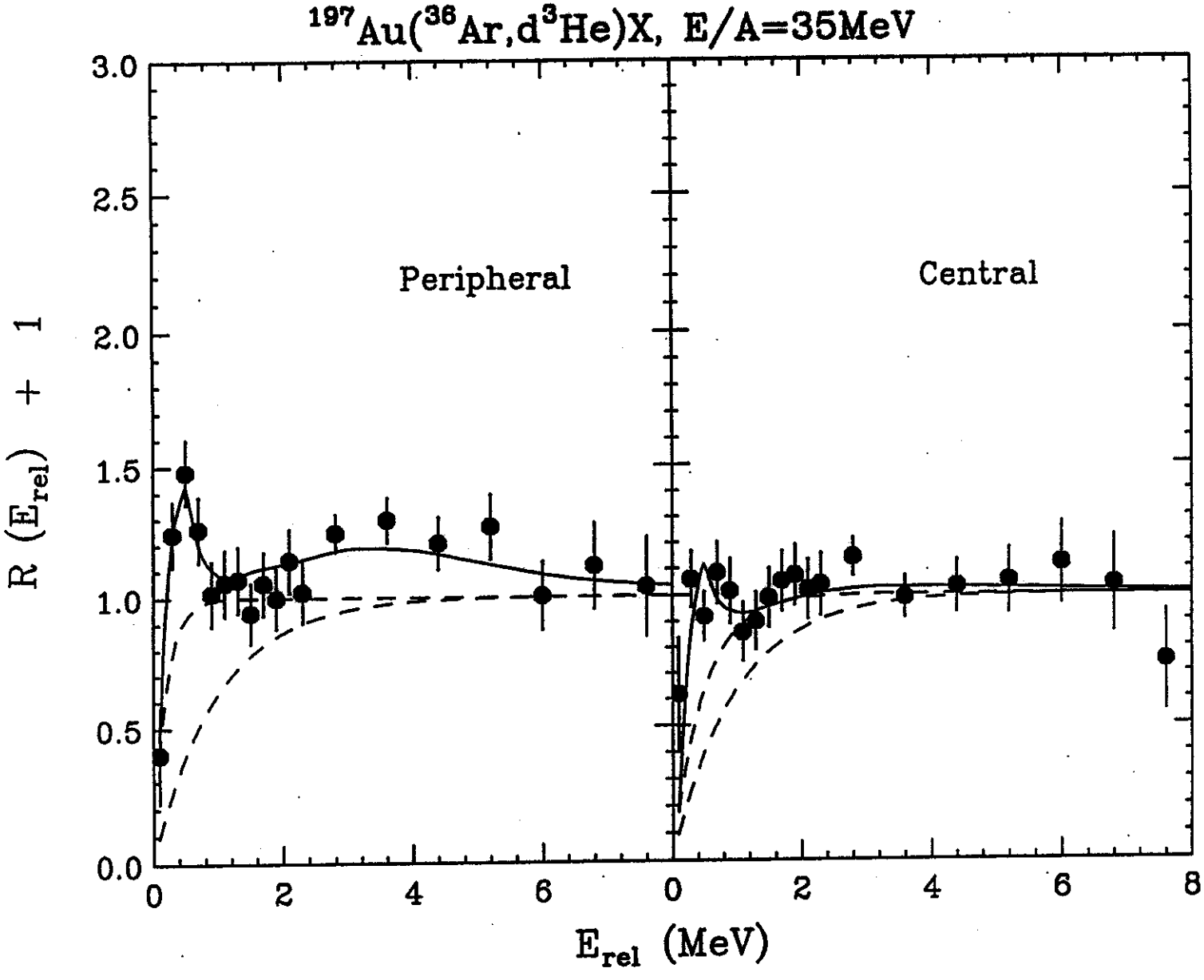
^{197}Au(^{36}Ar,d^{3}He)X, E/A=35MeV
Peripheral
Central
R (E$_{rel}$) + 1
E$_{rel}$ (MeV)
3.0
2.5
2.0
1.5
1.0
0.5
0.0
0
2
4
6
8

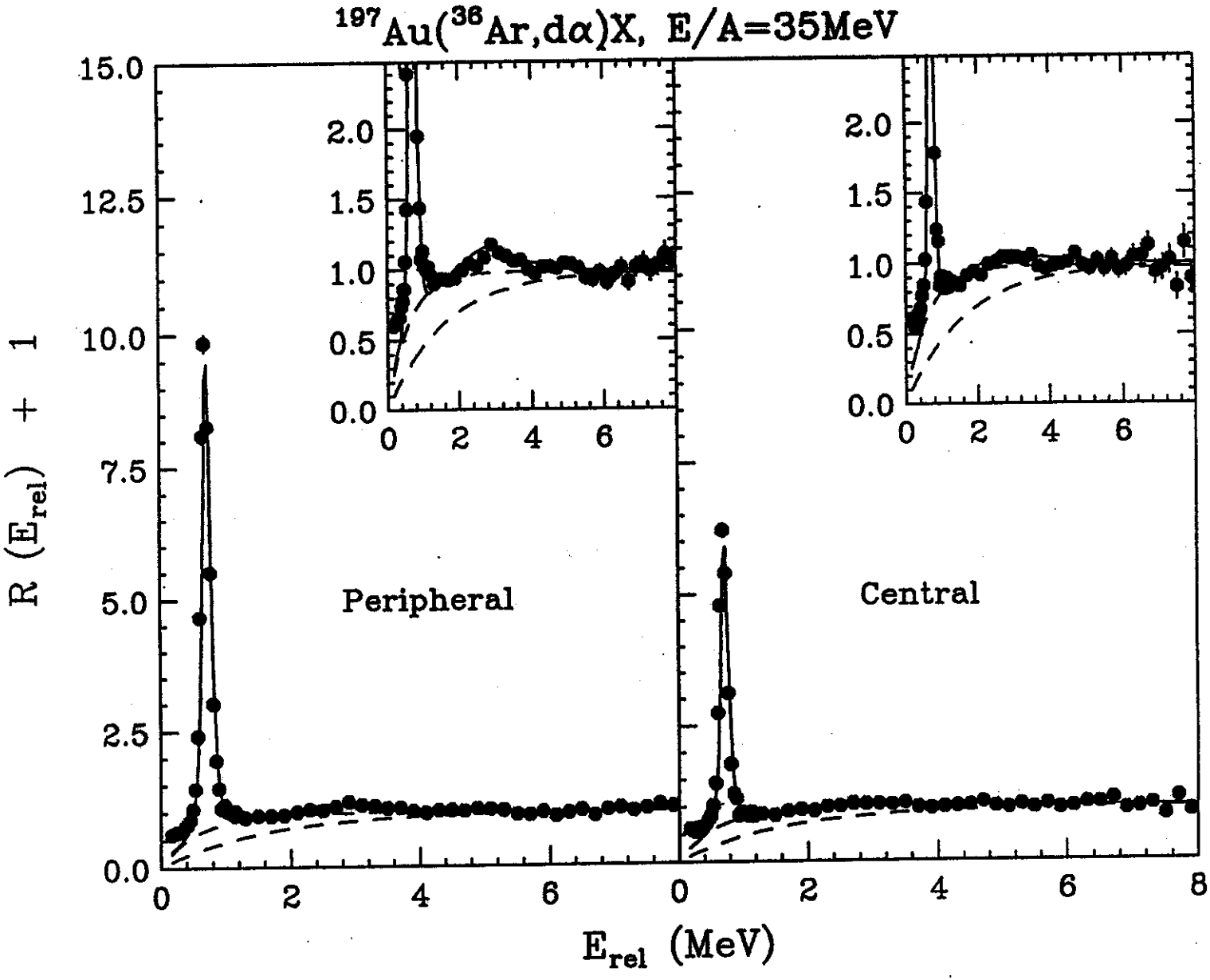
^{197}Au(^{36}Ar,dα)X, E/A=35MeV
R (E$_{rel}$) + 1
E$_{rel}$ (MeV)
Peripheral
Central
15.0
12.5
10.0
7.5
5.0
2.5
0.0
0
2
4
6
8
2.0
1.5
1.0
0.5
0.0

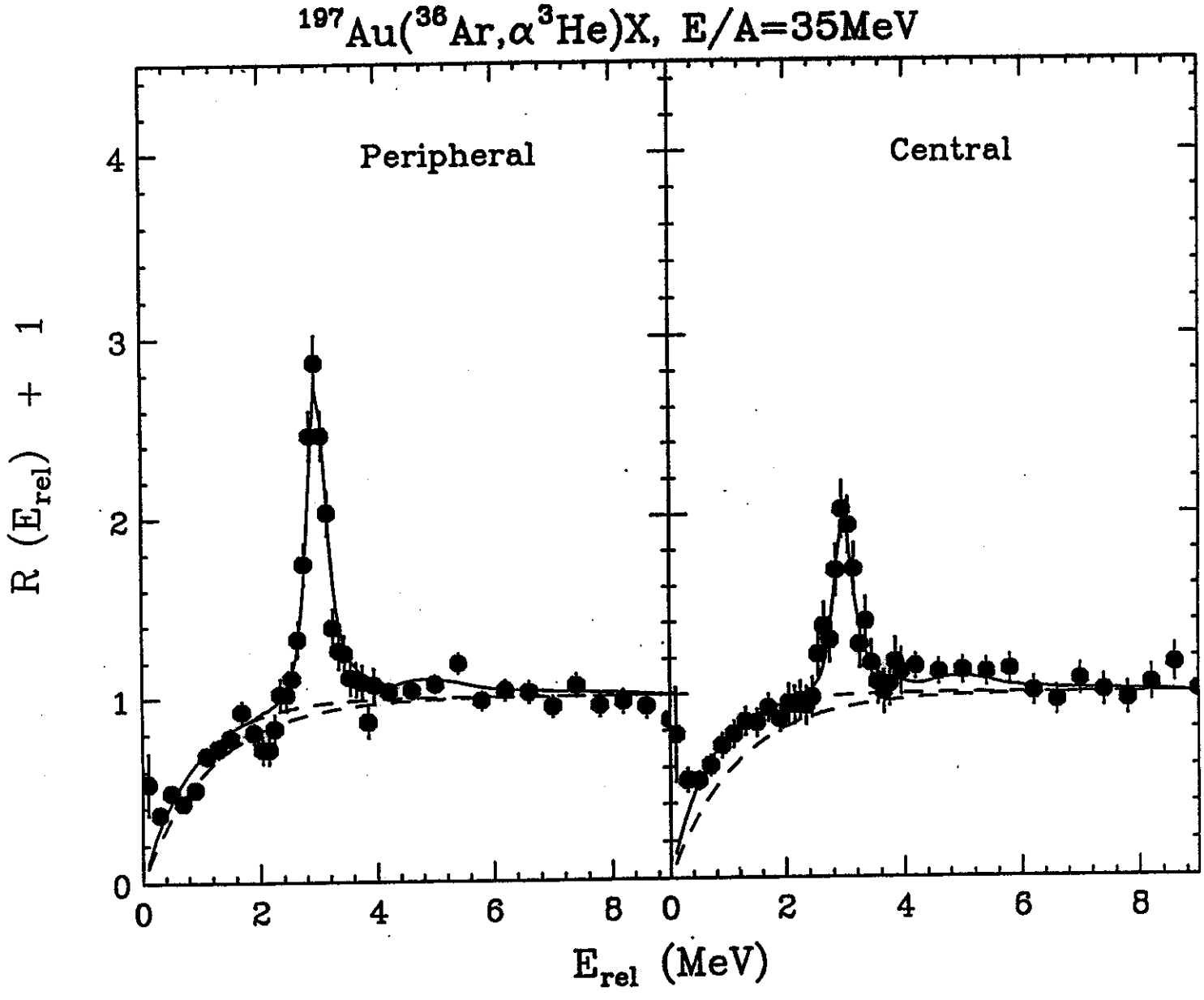
^{197}Au(^{36}Ar,α^{3}He)X, E/A=35MeV
Peripheral
Central
R (E_{rel}) + 1
E_{rel} (MeV)
0
1
2
3
4
0
2
4
6
8

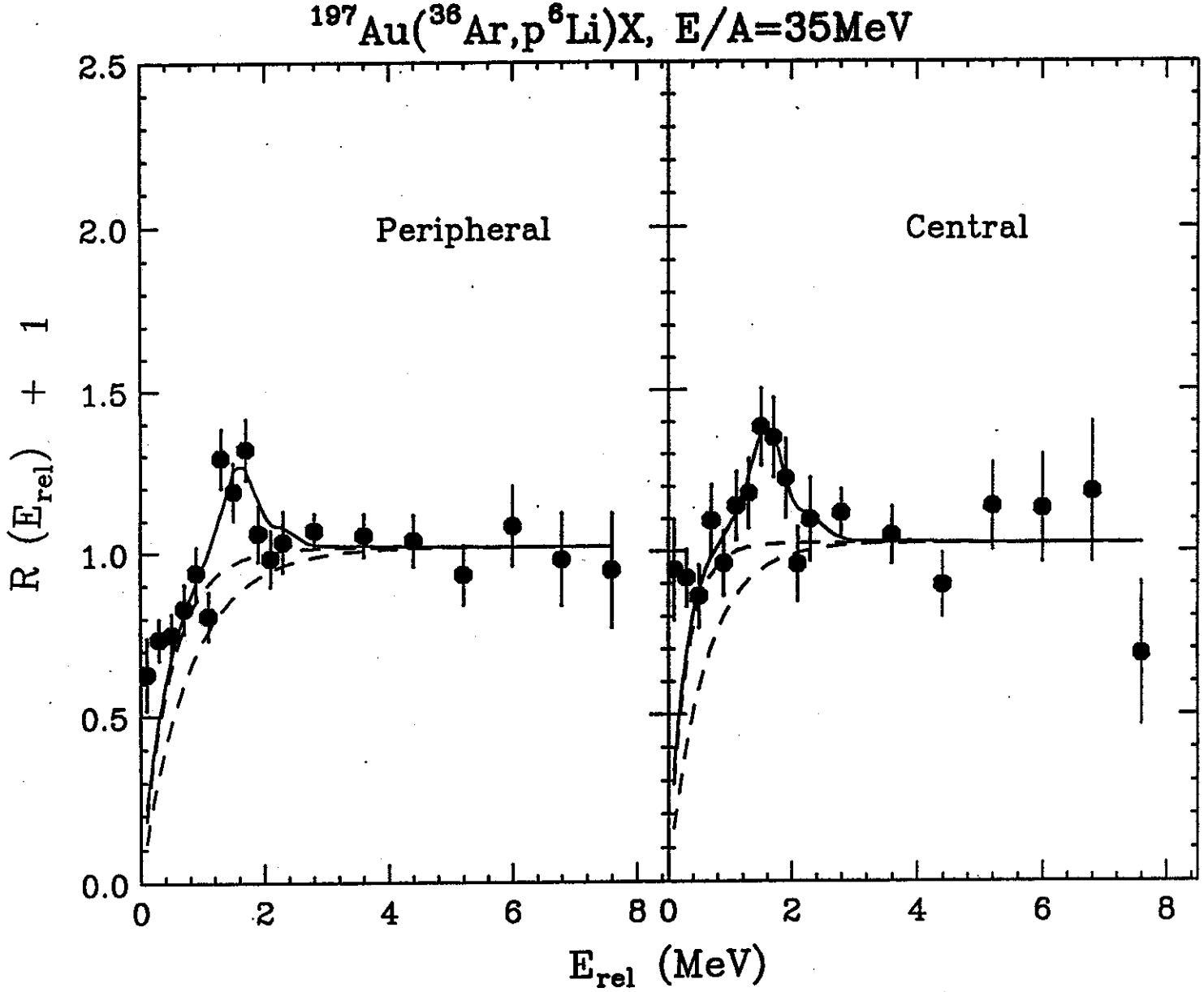
^{197}Au(^{36}Ar,p^{6}Li)X, E/A=35MeV
Peripheral
Central
R (E$_{rel}$) + 1
E$_{rel}$ (MeV)
0.0
0.5
1.0
1.5
2.0
2.5
0
2
4
6
8

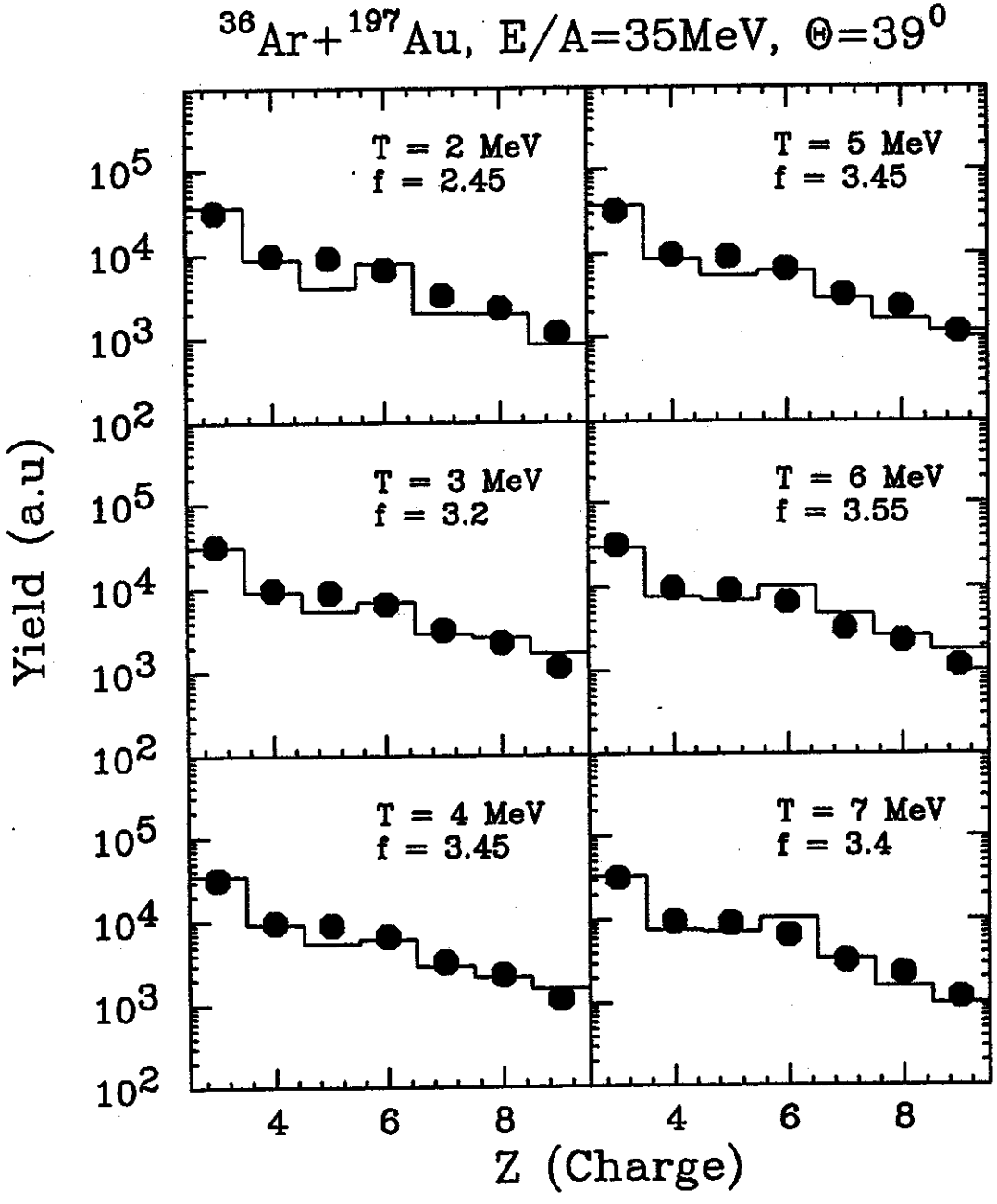
$^{36}Ar+^{197}Au$, E/A=35MeV, Θ=39^0
T = 2 MeV
f = 2.45
T = 5 MeV
f = 3.45
T = 3 MeV
f = 3.2
T = 6 MeV
f = 3.55
T = 4 MeV
f = 3.45
T = 7 MeV
f = 3.4
Yield (a.u)
10^5
10^4
10^3
10^2
4
6
8
Z (Charge)

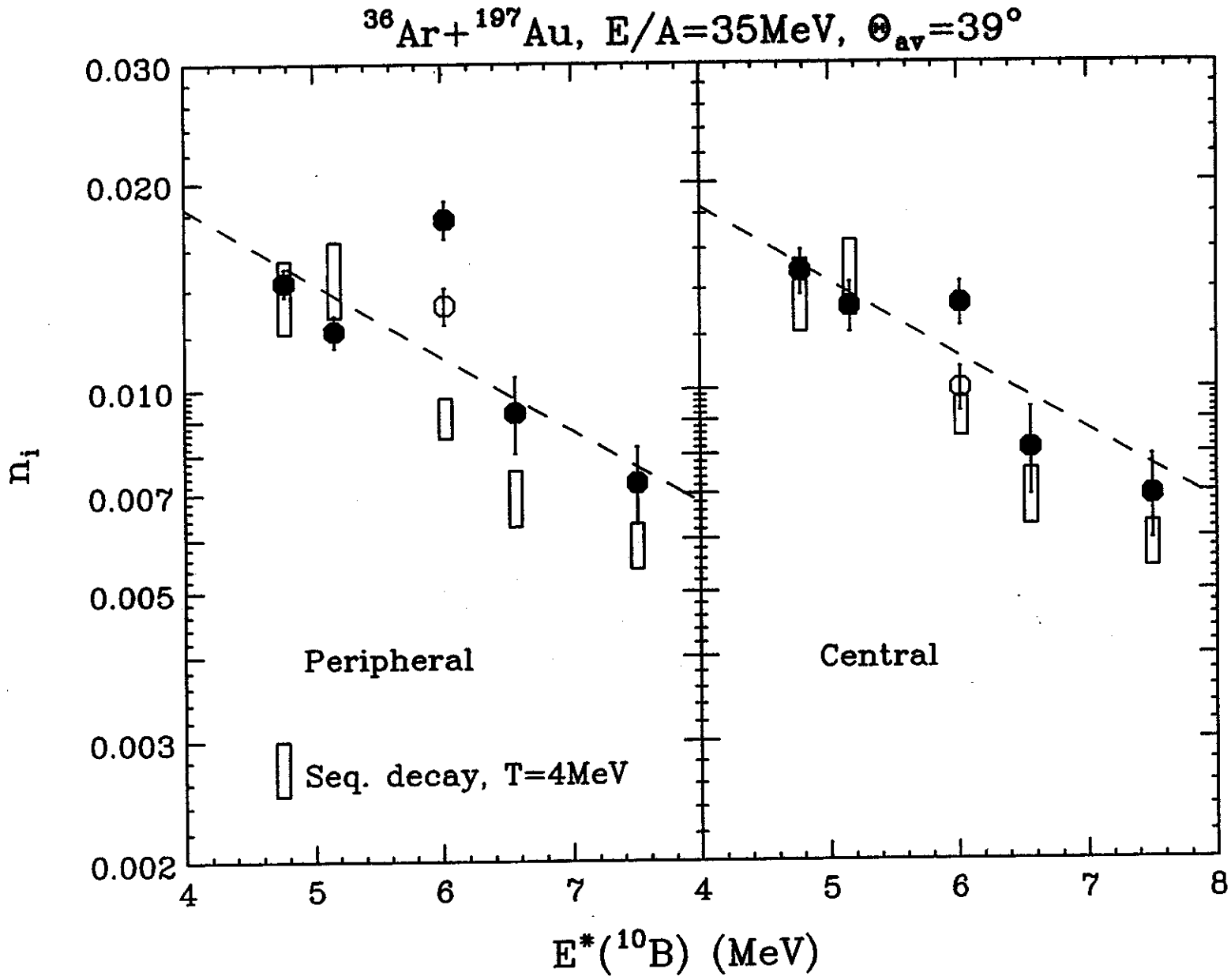
$^{36}Ar+^{197}Au$, E/A=35MeV, Θ_{av}=39°
0.030
0.020
0.010
0.007
0.005
0.003
0.002
n_i
Peripheral
Central
Seq. decay, T=4MeV
4
5
6
7
4
5
6
7
8
$E^*(^{10}B)$ (MeV)

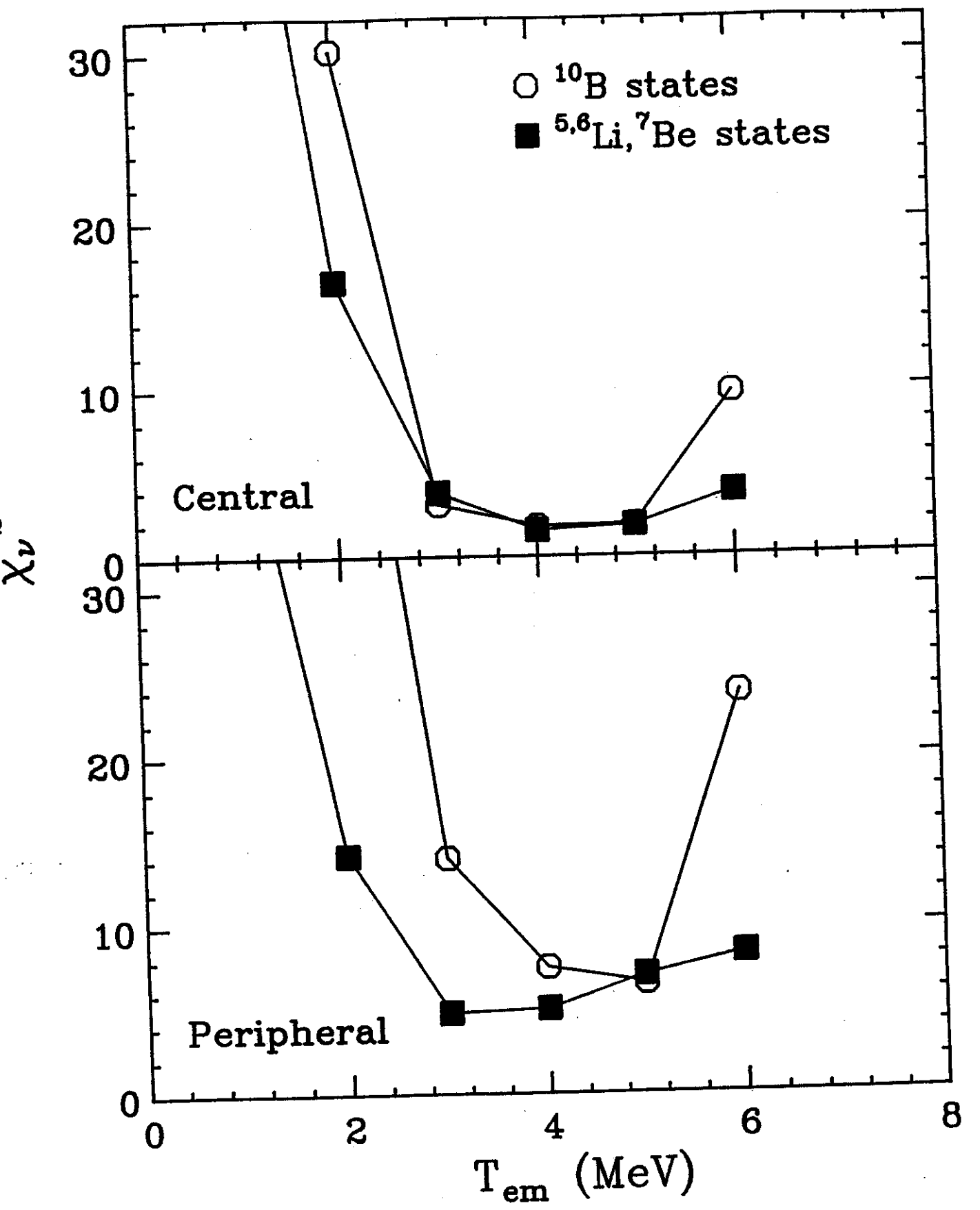
30
20
10
0
^{10}B states
^{5,6}Li,^{7}Be states
Central
30
20
10
0
Peripheral
0
2
4
6
8
T_{em} (MeV)
χ_ν

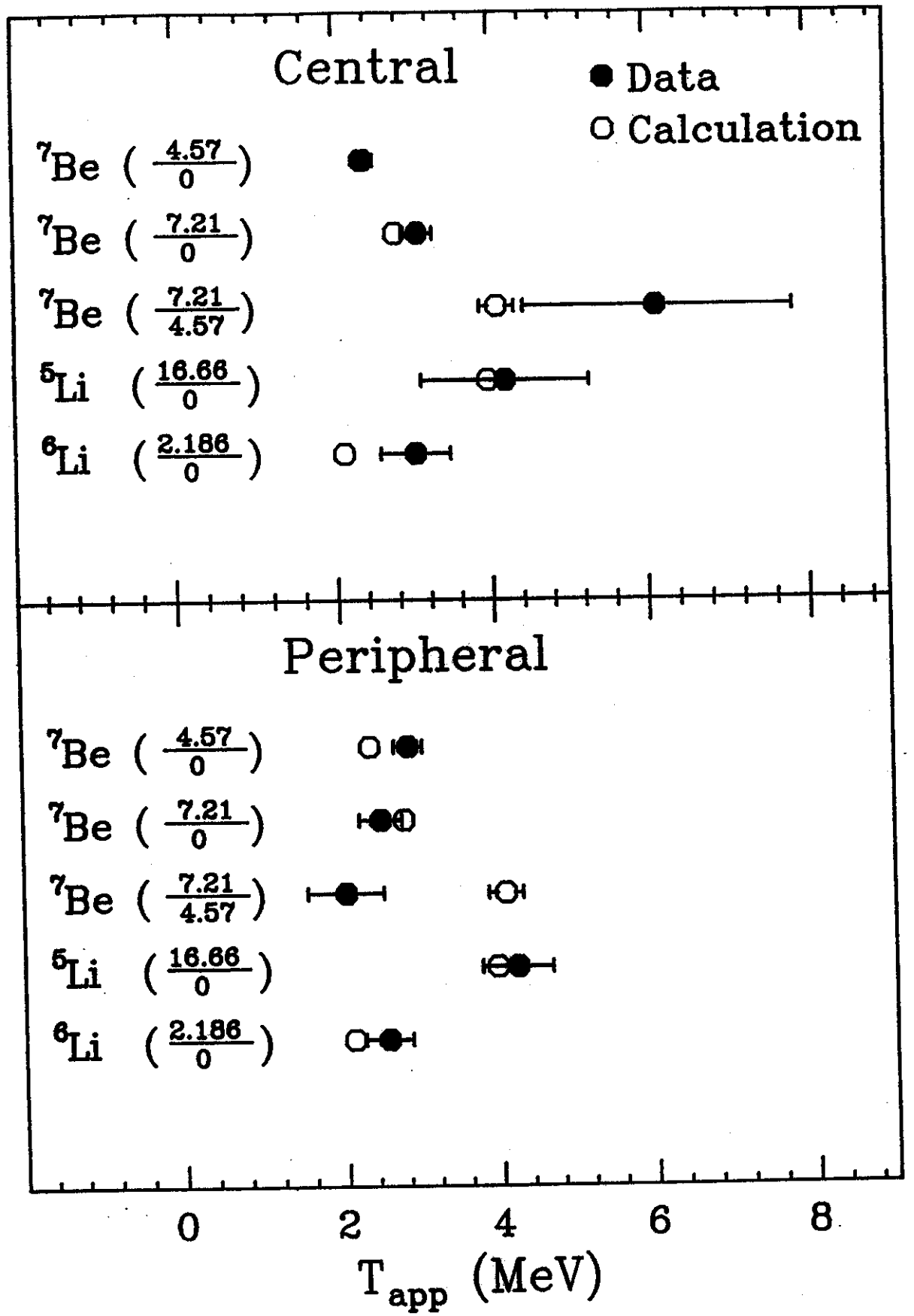
Central
Data
Calculation
^{7}Be (4.57 / 0)
^{7}Be (7.21 / 0)
^{7}Be (7.21 / 4.57)
^{5}Li (16.66 / 0)
^{6}Li (2.186 / 0)
Peripheral
^{7}Be (4.57 / 0)
^{7}Be (7.21 / 0)
^{7}Be (7.21 / 4.57)
^{5}Li (16.66 / 0)
^{6}Li (2.186 / 0)
0
2
4
6
8
T_{app} (MeV)